The Astrophysical Journal, 922:161 (17pp), 2021 December 1 https://doi.org/10.3847/1538-4357/ac1118

Forced Linear Shear Flows with Rotation: Rotating Couette–Poiseuille Flow, Its Stability, and Astrophysical Implications

Subham Ghosh and Banibrata Mukhopadhyay
Department of Physics, Indian Institute of Science, Bangalore 560012, India; subham@iisc.ac.in, bm@iisc.ac.in
Received 2021 April 12; revised 2021 July 2; accepted 2021 July 2; published 2021 November 29

Abstract

We explore the effect of forcing on the linear shear flow or plane Couette flow, which is also the background flow in the very small region of the Keplerian accretion disk. We show that depending on the strength of forcing and boundary conditions suitable for the systems under consideration, the background plane shear flow, and hence the accretion disk velocity profile, is modified into parabolic flow, which is a plane Poiseuille flow or Couette–Poiseuille flow, depending on the frame of reference. In the presence of rotation, the plane Poiseuille flow becomes unstable at a smaller Reynolds number under pure vertical as well as three-dimensional perturbations. Hence, while rotation stabilizes the plane Couette flow, the same destabilizes the plane Poiseuille flow faster and hence the forced local accretion disk. Depending on the various factors, when the local linear shear flow becomes a Poiseuille flow in the shearing box due to the presence of extra force, the flow becomes unstable even for Keplerian rotation, and hence turbulence will ensue. This helps to resolve the long-standing problem of subcritical transition to turbulence in hydrodynamic accretion disks and the laboratory plane Couette flow.

Unified Astronomy Thesaurus concepts: Accretion (14); Hydrodynamics (1963); Compact objects (288); Astrophysical fluid dynamics (101)

1. Introduction

Accretion disks are very exotic astrophysical objects. They are formed around a denser and heavier object, mainly in the form of a disk due to the accretion of matter from the surroundings. We are particularly interested in the region where the gravitational force almost balances the centrifugal force. This region is called the Keplerian region, and the flow therein is called the Keplerian flow. This flow is stable under linear perturbation, and this stability is called Rayleigh stability.

Nevertheless, to explain the observed physical quantities such as temperature, luminosity, etc. based on Keplerian disks (see, e.g., Frank et al. 2002), the flow therein must be assumed to be turbulent. Otherwise, there will be a mismatch of physical quantities, e.g., temperature, on some order of magnitude between theory and observations. Shakura & Sunyaev (1973) and Lynden-Bell & Pringle (1974) then proposed the idea of turbulent viscosity, which is responsible for the transport of matter inward in accretion disks and hence the physical observables. However, the reason behind the turbulence was not known until Balbus & Hawley (1991) proposed an idea of instability involving the coupling between the rotation of fluid and the weak magnetic field therein, following Velikhov (1959) and Chandrasekhar (1960). This instability is known as magnetorotational instability (MRI), which could bring nonlinearity into the system and hence turbulence. Later, Ogilvie & Pringle (1996) investigated MRI based on a more complicated analysis. Although MRI succeeds greatly in explaining the origin of turbulence in most of the hot flows, it fails to explain the same in several sites, e.g., protoplanetary disk (Bai 2017, 2013), cataclysmic variables in their low states (Gammie & Menou 1998; Menou 2000), the outer part of active galactic nucleus (AGN) disks, and the underlying dead zone (Menou & Quataert 2001). MRI is suppressed in these cases due to the very low ionization of the matter therein. In addition, the systems with huge Reynolds number ($\gtrsim 10^9$), as argued by Nath & Mukhopadhyay (2015), have a higher growth rate due to magnetic transient growth than the growth rate due to MRI. Bhatia & Mukhopadhyay (2016), however, showed that even transient energy growth ceases to occur beyond a certain magnetic field in magnetohydrodynamical shear flows. Pessah & Psaltis (2005) and Das et al. (2018), using local and global analysis respectively, showed the stabilization of the axisymmetric MRI above a certain magnitude of the toroidal component of the magnetic field for compressible and differentially rotating flows. All these publications showed that MRI is not a generic way to make the Keplerian flow unstable and hence turbulent. As hydrodynamics is generically there, it is worth looking for plausible hydrodynamic instability instead.

However, the Keplerian flow is Rayleigh stable, and there is a long debate in the literature (Dauchot & Daviaud 1995; Richard & Zahn 1999; Kim & Ostriker 2000; Rüdiger & Zhang 2001; Klahr & Bodenheimer 2003; Yecko 2004; Dubrulle et al. 2005a, 2005b; Mahajan & Krishan 2008; Mukhopadhyay et al. 2011; Mukhopadhyay & Chattopadhyay 2013) regarding the stability of Rayleigh-stable flows, especially in the context of accretion disks. The authors put forward their efforts to resolve this issue either analytically, with a simulation, or experimentally. For instance, Balbus et al. (1996) and Hawley et al. (1999) concluded that the sustained turbulence was not possible in the Keplerian flow from hydrodynamics. Nevertheless, other authors, such as Lesur & Longaretti (2005), strongly disagreed with this and discussed the unavailability of computer resources to resolve the Keplerian regime. However, with their extrapolated numerical data, they could not produce astrophysically sufficient subcritical turbulent transport in a Keplerian flow. Other authors have also argued for a plausible emergence of hydrodynamical instability and hence further turbulence by transient growth in the case of otherwise linearly stable flows (e.g., Chagelishvili et al. 2003; Tevzadze et al. 2003; Afshordi et al. 2005; Mukhopadhyay et al. 2011, 2005; Cantwell et al. 2010) in laboratory experiments (e.g., Paoletti et al. 2012) and in simulations in case of accretion disks (e.g., Avila 2012).

We therefore look for hydrodynamics that could plausibly give rise to unstable modes when the dynamics of the fluid parcel is studied in a small cubical shearing box (see, e.g., Mukhopadhyay et al. 2005; Ghosh & Mukhopadhyay 2020, for details) situated at a particular radius in the Keplerian disk. We are particularly motivated and inspired by our recent results (Ghosh & Mukhopadhyay 2020), which explored in detail the effect of forcing in the linearly and nonlinearly perturbed plane shear flows, with and without rotation, which shed light on the issue of the origin of hydrodynamical turbulence. In fact, other works (Ioannou & Kakouris 2001; Mukhopadhyay & Chattopadhyay 2013; Nath & Mukhopadhyay 2016; Razdoburdin 2020) have considered an extra forcing to be present in the system. However, in the shearing box, the background flow has a linear shear profile up to first-order approximation (see Appendix and Balbus et al. 1996, for details). This linear shear flow is called the plane Couette flow. As in the accretion disk, the shearing box is situated at a particular radius, it will have an angular frequency. We therefore have to consider the effect of rotation while we describe the motion of the accretion disk fluid parcel inside the shearing box. Now, if an extra force is present there in the shearing box, the background flow no longer remains linear shear, but instead becomes quadratic shear flow what we generally call plane Couette–Poiseuille flow. However, with a proper transformation, this flow can be transformed into plane Poiseuille flow. This flow will further be embedded with rotation in the context of Keplerian flow. Plane Poiseuille flow without rotation is unstable under linear two-dimensional perturbation, having a critical Reynolds number 5772.22 with a critical wavevector 1.02 (Orszag 1971). Once it is established that the very local flow (inside the box) in the Keplerian region with forcing is plane Poiseuille flow with rotation, then we can argue that the flow inside the shearing box is unstable. We therefore plan to explore plane Poiseuille flow in the presence of a rotational effect. Although the effect of rotation on the stability of a Poiseuille flow was studied by Lezius & Johnston (1976) and Alfredsson & Persson (1989), our work is different form theirs in two aspects. First, we extensively study the eigenspectra of a plane Poiseuille flow, as well as a Couette–Poiseuille flow, with rotation for purely vertical perturbations and three-dimensional perturbations. To the best of our knowledge, this study has not been done in an extensive manner yet, particularly for the effect of rotation on the stability analysis of a Couette–Poiseuille flow. Although the Poiseuille flow in the presence of rotation has been studied earlier, to our knowledge, its application to the stability of accretion flow has never been explored. In addition, no analysis of eigenspectra for a Poiseuille flow in the presence of rotation has been performed extensively so far. However, see, e.g., Hains (1967), Cowley & Smith (1985), Balakumar (1997), Savenkov (2010), and Klotz et al. (2017) for various explorations of the Couette–Poiseuille flow over the years. Second, the background flow profile that we consider here is different than those already considered in previous works (see Lezius & Johnston 1976; Alfredsson & Persson 1989, for details).

The plan of the paper is the following. In Section 2 we show how the linear shear flow (or plane Couette flow) is modified by the presence of an extra force in the system. In a recent work, we assumed that the background does not practically change due to forcing (Ghosh & Mukhopadhyay 2020), here, however, we explore the change in background and its consequence in detail. As the background modifies in the presence of the extra force, the domain of the background also modified depending on the strength of the force. The relevance of the size of the new domain

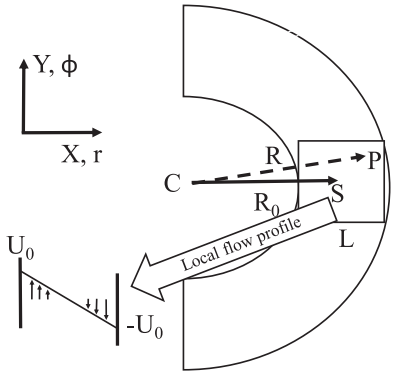

Figure 1. Schematic diagram of a shearing box centered at the point S inside the small patch of an accretion disk. The box is of size L. C is the center of the accretion disk. S is at a distance R_0 from C. An arbitrary fluid particle inside the box is at P at a distance R from C.

is studied in Section 3. We write the Navier–Stokes equation for the modified background flow in the rotating frame, as the primary plan is the application in accretion disks, in Section 4, and we also obtain the corresponding Reynolds number after nondimensionalizing it in Section 4.1. The perturbed flow equations have been formulated appropriately in the same section, but in Section 4.2, where we recast the Navier–Stokes equation into Orr–Sommerfeld and Squire equations. Rotating Poiseuille and Couette–Poiseuille flows under purely vertical and three-dimensional perturbations are explored in detail in Section 5 and Section 6, respectively. The dependens of the stability of the respective flows on the rotational profile is also studied in the same sections. In Section 7 we describe the accuracy of our numerical results based on the technique we have used in this work. In Section 8 we compare plane Poiseuille flow with plane Couette flow in the presence of rotation. In the same section, we also compare our critical parameters with those in the literature. We finally conclude in Section 9 that depending on the boundary conditions and the strength of the extra force, there is a deviation in the flow from its linear shear nature. Furthermore, rotation makes the flow unstable depending on the parameters, and hence the flow plausibly becomes turbulent, which we suggest to be the hydrodynamical origin of turbulence in accretion disks.

2. Background Flow in the Presence of Force

Let us consider a very small cubical box of size L at a particular radius R_0 from the center of the system, as shown in Figure 1. At this radius, the box is rotating with an angular frequency Ω_0 such that $\Omega = \Omega_0(R/R_0)^{-q}$ and the rotation parameter $q = 3/2$ for Keplerian flow. In Figure 1, S is the center of the box, and the local analysis is done with respect to S. See Mukhopadhyay et al. (2005), Bhatia & Mukhopadhyay (2016), and Ghosh & Mukhopadhyay (2020) for details of the reference frame and the background flow therein. Now let us set the local reference frame or box in such a way that the flow, which is along the ϕ-direction with respect to C, is in the y-direction, and either ends of the box in the x-direction (in the disk frame r-direction) have an equal and opposite velocity of magnitude U_0 (see Figure 1 of Ghosh & Mukhopadhyay 2020). In this local reference frame or box, the velocity of the Keplerian flow becomes $-q\Omega_0 X$ up to the first-order approximation. This is the usual background flow (see the Appendix and also Hawley et al. 1995; Afshordi et al. 2005; Mukhopadhyay et al. 2005; Ghosh & Mukhopadhyay 2020)

in the local region of an accretion disk. However, due to the presence of an external force (may not be random) in the flow, the above-mentioned background flow is expected to change. The various possible origins of force in the system under consideration, as described earlier by us (Ghosh & Mukhopadhyay 2020) in detail, could be back-reactions of an outflow/jet to accretion disks, the interaction between the dust grains and fluid parcel in protoplanetary disks, etc. Using fluid-particle interactions, these possibilities could be modeled in such a way that the extra force turns out to be a function of the relative velocity between the fluid and the particles. For details, see Section 2.1 and Appendix A of Ghosh & Mukhopadhyay (2020). In the presence of an extra force, let us consider the background flow velocity to be $\boldsymbol{V}$, given by

$$\boldsymbol{V} = (0,\ V_Y(X),\ 0). \tag{1}$$

The corresponding Navier–Stokes equation describing the flow in the local box is

$$\frac{\partial \boldsymbol{V}}{\partial t} + (\boldsymbol{V}\cdot\boldsymbol{\nabla})\boldsymbol{V} = -\frac{\boldsymbol{\nabla} P}{\rho} + \nu\nabla^2\boldsymbol{V} + \boldsymbol{\Gamma}, \tag{2}$$

where P, ρ, ν, and $\boldsymbol{\Gamma}$ are the pressure, density, kinematic viscosity, and extra force, respectively. The three components of Equation (2) are

$$0 = -\frac{1}{\rho}\frac{\partial P}{\partial X} + \Gamma_X, \tag{3}$$

$$0 = -\frac{1}{\rho}\frac{\partial P}{\partial Y} + \nu\nabla^2 V_Y + \Gamma_Y, \tag{4}$$

$$0 = -\frac{1}{\rho}\frac{\partial P}{\partial Z} + \Gamma_Z. \tag{5}$$

Equation (4) can be further simplified to

$$\begin{aligned}\nabla^2 V_Y &= \frac{1}{\nu}\left(-\Gamma_Y + \frac{1}{\rho}\frac{\partial P}{\partial Y}\right) = \frac{\partial^2 V_Y}{\partial X^2}\\ \Rightarrow V_Y &= -\left(\frac{\Gamma_Y}{\nu} - \frac{1}{\nu\rho}\frac{\partial P}{\partial Y}\right)\frac{X^2}{2} + C_1 X + C_2\\ &= -K\frac{X^2}{2} + C_1 X + C_2,\end{aligned} \tag{6}$$

where

$$K = \left(\frac{\Gamma_Y}{\nu} - \frac{1}{\nu\rho}\frac{\partial P}{\partial Y}\right), \tag{7}$$

is assumed to be constant.

The corresponding boundary conditions are given by

$$V_Y = \mp U_0 \text{ at } X = \pm L, \tag{8}$$

which imply that $C_1 = -U_0/L$ and $C_2 = KL^2/2$. The background flow in the presence of extra force is therefore modified and becomes

$$V_Y = \frac{K}{2}(L^2 - X^2) - \frac{U_0 X}{L}, \tag{9}$$

which is the Couette–Poiseuille flow, when linear and nonlinear shears are both present. By a simple rearrangement, this reduces to

$$V_Y = \alpha(1 - \mathcal{X}^2), \tag{10}$$

where

$$\begin{aligned}\mathcal{X}^2 &= \frac{K}{2}\frac{\Upsilon^2}{\alpha},\ \Upsilon^2 = \left(X + \frac{U_0}{KL}\right)^2\\ \text{and } \alpha &= \frac{U_0^2}{2KL^2} + \frac{L^2 K}{2}.\end{aligned} \tag{11}$$

The velocity V_Y in Equation (10) can be made dimensionless by dividing it with α, i.e.,

$$U_{\alpha Y} = \frac{V_Y}{\alpha} = 1 - \mathcal{X}^2, \tag{12}$$

where α is the dimension of velocity, determined by the box geometry. The new background flow therefore becomes $\boldsymbol{U}_\alpha = (0,\ U_{\alpha Y},\ 0)$. However, this is the plane Poiseuille flow in new coordinates $(\mathcal{X},\ Y,\ Z)$, where the boundary conditions are given by Equation (8). Note that here $\mathcal{X}$ is dimensionless, while Y and Z are dimensionful coordinates. Nevertheless, it is useful to solve the problem within the known domain of the Poiseuille flow, i.e., $\mathcal{X} \in [-1,\ 1]$, in which it is known to be unstable above a certain Reynolds number (Re).

3. The New Domain

In order to employ the results of the well-known Poiseuille flow, we set the boundary conditions to new coordinates: $\boldsymbol{U}_\alpha = 0$ at $\mathcal{X} = \pm 1$. It is therefore important to verify the consequence of the domain of $\mathcal{X}$ (i.e., running from -1 to 1) to the domain of X (i.e., running from $-L$ to L), as chosen originally. From Equation (11), imposing $\mathcal{X} = \pm 1$, we have

$$X = \pm\sqrt{\frac{2\alpha}{K}} - \frac{U_0}{KL}, \tag{13}$$

where

$$\sqrt{\frac{2\alpha}{K}} = L\sqrt{\left(1 + \frac{U_0^2}{K^2L^4}\right)}. \tag{14}$$

Now if $U_0^2/K^2L^4 \ll 1$, Equation (14) shows that

$$\sqrt{\frac{2\alpha}{K}} \cong L + \frac{U_0^2}{2K^2L^3}, \tag{15}$$

leading to

$$X = \pm L - \frac{U_0}{KL} \pm \frac{U_0^2}{2K^2L^3}. \tag{16}$$

This confirms that the domain size of X is close to $2L$ if $U_0^2/K^2L^4 \ll 1$, i.e., $\nu^2 U_0^2/L^4 \ll \Gamma_Y^2$, when the flow is not driven by the pressure, i.e., $\partial P/\partial Y = 0$. However, in the presence of a pressure gradient, the same condition will be true, but its contribution will be added to the extra force.

However, if $U_0^2/K^2L^4 \gg 1$, Equation (14) shows that

$$\sqrt{\frac{2\alpha}{K}} \cong \frac{U_0}{KL}. \tag{17}$$

Hence

$$X = \pm\frac{U_0}{KL} - \frac{U_0}{KL}, \tag{18}$$

i.e., the domain size of X is approximately $2U_0/KL$. According to the approximation $U_0^2/K^2L^4 \gg 1$, $2U_0/KL$ is much larger

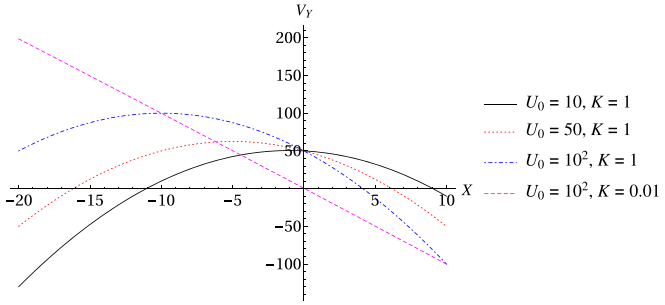

Figure 2. Modification of the background flow in the presence of a constant extra force shown against the flow variable X for various cases of parameters U_0 and K, when $L = 10$.

than $2L$. Hence, the domain increases compared to what was chosen originally. Therefore our original choice of a small Cartesian patch in the flow may violate this choice. This may further create a problem for the application to accretion disks, which is described below in detail.

Figure 2 shows the modified background flow in the presence of a constant extra force for various U_0 and K with $L = 10$. It is clear that for $U_0 = 10$ and $K = 1$, the new domain size almost remains same as $2L = 20$, because $U_0^2/K^2L^4 = 10^{-2} \ll 1$. However, when U_0 increases, keeping K fixed, the domain size also increases. All these cases show the parabolic background flows in which the focus changes from (0, 0) to $(-U_0/KL, 0)$. Interestingly, if we keep decreasing K, keeping U_0 fixed, the linear background velocity eventually emerges again, as the extra force is negligible in this case (see Equation (10)).

The approximation $U_0^2/K^2L^4 \ll 1$ is therefore more suitable for our problem as it leads to almost the same domain size, $2L$, as was chosen originally.

4. Navier–Stokes Equation in a Rotating Frame

Now our primary interest is to understand stability of rotating shear flows, particularly in the context of accretion disks. Hence, the plan is to examine the stability of the background flow with velocity $\boldsymbol{U}_\alpha$ within the new domain, i.e., $\mathcal{X} \in [-1, 1]$, as discussed in Section 3, which is rotating with respect to the center of the system at R_0. Before doing so, we have to establish suitable equations depending on the reference frame and make them dimensionless for convenience. This exploration is essentially the stability analysis of a plane Poiseuille flow in the presence of rotation, here particularly the Coriolis effect. We eventually obtain a dimensionless number characterizing the flow to be laminar or turbulent in the domain of interest, i.e., the Reynolds number in the new coordinate system $(\mathcal{X}, Y, Z)$, which is Re_α.

4.1. Defining the Reynolds Number in a Local Region

Let us consider the local Cartesian frame or box at radius R_0, as shown by Figure 1, rotating with the angular velocity $\boldsymbol{\omega} = (0, 0, \Omega_0)$ such that $\Omega = \Omega_0(R/R_0)^{-q}$, where $\Omega_0 = V_Y(\mathcal{X} = 0)/(qL_{ch}/2) = 2\alpha\sqrt{K}/q\sqrt{2\alpha} = \alpha\sqrt{2K}/q\sqrt{\alpha}$, L_{ch} is the characteristic length scale of the system. The Navier–Stokes equation in this frame is

$$\frac{\partial \boldsymbol{V}}{\partial t'} + (\boldsymbol{V}\cdot\boldsymbol{\nabla})\boldsymbol{V} + \boldsymbol{\omega}\times\boldsymbol{\omega}\times\boldsymbol{D} + 2\boldsymbol{\omega}\times\boldsymbol{V} + \frac{\boldsymbol{\nabla}P}{\rho} = \nu\nabla^2\boldsymbol{V} + \boldsymbol{\Gamma}, \tag{19}$$

where the position vector $\boldsymbol{D} = (X, Y, Z)$, and $\boldsymbol{\nabla} = (\partial/\partial X, \partial/\partial Y, \partial/\partial Z)$ in Cartesian coordinates. If we divide both sides of Equation (19) by α, we obtain an equation for $\boldsymbol{U}_\alpha$, which is given by

$$\frac{\partial \boldsymbol{U}_\alpha}{\partial t'} + \alpha(\boldsymbol{U}_\alpha\cdot\boldsymbol{\nabla})\boldsymbol{U}_\alpha + \boldsymbol{\omega}\times\boldsymbol{\omega}\times\frac{\boldsymbol{D}}{\alpha} + 2\boldsymbol{\omega}\times\boldsymbol{U}_\alpha + \boldsymbol{\nabla}P_\alpha = \nu\nabla^2\boldsymbol{U}_\alpha + \boldsymbol{\Gamma}_\alpha, \tag{20}$$

where $P_\alpha = P/\rho\alpha$ and $\boldsymbol{\Gamma}_\alpha = \boldsymbol{\Gamma}/\alpha$. We now redefine the variables in terms of dimensionless quantities, i.e., $t' \to \sqrt{2/\alpha K}\,t$, $(X, Y, Z) \to \sqrt{2\alpha/K}\,(\mathcal{X}, y, z)$, where $\boldsymbol{d} = (\mathcal{X}, y, z)$, and $\boldsymbol{\nabla} \to \sqrt{K/2\alpha}\,\boldsymbol{\nabla}_\alpha$, where $\boldsymbol{\nabla}_\alpha = (\partial/\partial\mathcal{X}, \partial/\partial y, \partial/\partial z)$. Hence, Equation (20) in terms of dimensionless variables, for an incompressible fluid, becomes

$$\frac{\partial \boldsymbol{U}_\alpha}{\partial t} + (\boldsymbol{U}_\alpha\cdot\boldsymbol{\nabla}_\alpha)\boldsymbol{U}_\alpha + \frac{1}{q^2}\hat{k}\times\hat{k}\times\boldsymbol{d} + \frac{2}{q}\hat{k}\times\boldsymbol{U}_\alpha + \frac{1}{\alpha}\boldsymbol{\nabla}_\alpha P_\alpha = \frac{\nu\sqrt{K}}{\alpha\sqrt{2\alpha}}\nabla_\alpha^2\boldsymbol{U}_\alpha + \Gamma'_\alpha. \tag{21}$$

The Reynolds number is therefore defined as

$$Re_\alpha = \frac{\alpha\sqrt{2\alpha}}{\nu\sqrt{K}} \tag{22}$$

and $\boldsymbol{\Gamma}'_\alpha = \boldsymbol{\Gamma}\sqrt{2/K\alpha^3}$.

4.2. Perturbation Analysis

Equation (21) along with

$$\boldsymbol{\nabla}_\alpha\cdot\boldsymbol{U}_\alpha = 0 \tag{23}$$

describes the dynamics of a fluid inside the local box. Now we perturb Equations (21) and (23) linearly and check whether the perturbation decays or grows with time. The velocity perturbation is $\boldsymbol{u}' = (u, v, w)$, the corresponding vorticity perturbation is $\boldsymbol{\nabla}\times\boldsymbol{u}'$, and the pressure perturbation is p'. After perturbing Equation (21), we eliminate the pressure term from the governing equation and recast it into the corresponding homogeneous Orr–Sommerfeld and Squire equations, which are given by

$$\left(\frac{\partial}{\partial t} + U_{\alpha Y}\frac{\partial}{\partial y}\right)\nabla_\alpha^2 u - U''_{\alpha Y}\frac{\partial u}{\partial y} + \frac{2}{q}\frac{\partial\zeta}{\partial z} - \frac{1}{Re_\alpha}\nabla_\alpha^4 u = 0, \tag{24}$$

$$\left(\frac{\partial}{\partial t} + U_{\alpha Y}\frac{\partial}{\partial y}\right)\zeta - U'_{\alpha Y}\frac{\partial u}{\partial z} - \frac{2}{q}\frac{\partial u}{\partial z} - \frac{1}{Re_\alpha}\nabla_\alpha^2\zeta = 0, \tag{25}$$

where ζ is the x-components of the vorticity perturbations, the prime denotes the differentiation with respect to $\mathcal{X}$, and the extra force Γ is assumed to remain the same under perturbation so that it is eliminated from the equation. If Γ would have been considered to be changed under perturbation, it would create an additional impact on the flow in order to reveal instability, as recently discussed by us (Ghosh & Mukhopadhyay 2020) in the context of linear shear. However, for the present purpose,

we plan to explore a minimum impact of force on the flow. Nevertheless, Equations (24) and (25) are the homogeneous part of the Orr–Sommerfeld and Squire equations, corresponding to the perturbation in Equation (21) (see Ghosh & Mukhopadhyay 2020, for inhomogeneous Orr–Sommerfeld and Squire equations due to the effect of force). The corresponding chosen no-slip boundary conditions are $u = v = w = 0$ at the two boundaries $\mathcal{X} = \pm 1$, or equivalently, $u = \frac{\partial u}{\partial \mathcal{X}} = \zeta = 0$ at $\mathcal{X} = \pm 1$. Hence, the linearized eigenspectra corresponding to Equation (21) will be described by Equations (24) and (25) only. The eigenspectra will not change due to the presence of the nonhomogeneous term arising due to the presence of the extra force. Our main aim here is to observe the changes in the eigenspectra those are caused by the changes in various flow properties. Note importantly that in principle, a small section of an accretion disk should not have any boundary, as imposed here in order to introduce the boundary condition for the solution purpose. However, the idea is that the entire disk, at least the region in which turbulence is sought for, is divided into small boxes, and if one box is unstable under perturbation, others will follow. All boxes are assumed to be arranged together. Hence, on either side of a boundary, the perturbation remains working intact in the respective boxes. Therefore, although boundaries are introduced for the solution purpose, this does not practically introduce any artifact for the present purpose. Nevertheless, Mukhopadhyay et al. (2005) and Afshordi et al. (2005) showed that the results practically do not depend on whether the analyses are based on the shearing sheet or shearing box.

5. Perturbation Analysis of a Rotating Poiseuille Flow

5.1. Three-dimensional Perturbation

In order to understand the evolution of linear perturbation, let the linear solutions be (e.g., Mukhopadhyay et al. 2005)

$$u = \hat{u}(\mathcal{X}, t) e^{i\boldsymbol{k}\cdot\boldsymbol{r}}, \tag{26}$$

$$\zeta = \hat{\zeta}(\mathcal{X}, t) e^{i\boldsymbol{k}\cdot\boldsymbol{r}}, \tag{27}$$

with $\boldsymbol{k} = (0,\ k_y,\ k_z)$ and $\boldsymbol{r} = (0,\ y,\ z)$. Substituting these in Equations (24) and (25), neglecting nonlinear terms, we obtain

$$\frac{\partial \hat{u}}{\partial t} + i(\mathcal{D}^2 - k^2)^{-1}\left[k_y U_{\alpha Y}(\mathcal{D}^2 - k^2) - k_y U''_{\alpha Y} - \frac{1}{iRe_\alpha}(\mathcal{D}^2 - k^2)^2\right]\hat{u} + (\mathcal{D}^2 - k^2)^{-1}\frac{2}{q} ik_z \hat{\zeta} = 0. \tag{28}$$

and

$$\frac{\partial \hat{\zeta}}{\partial t} + ik_y U_{\alpha Y}\hat{\zeta} - \left(U'_{\alpha Y} + \frac{2}{q}\right) ik_z \hat{u} - \frac{1}{Re_\alpha}(\mathcal{D}^2 - k^2)\hat{\zeta} = 0, \tag{29}$$

where $\mathcal{D} = \frac{\partial}{\partial \mathcal{X}}$.

Further combining Equations (28) and (29), we obtain

$$\frac{\partial}{\partial t} Q + i\mathcal{L}Q = 0, \tag{30}$$

where

$$Q = \begin{pmatrix} \hat{u} \\ \hat{\zeta} \end{pmatrix},\ \mathcal{L} = \begin{pmatrix} \mathcal{L}_{11} & \mathcal{L}_{12} \\ \mathcal{L}_{21} & \mathcal{L}_{22} \end{pmatrix}, \tag{31}$$

$$\begin{aligned} \mathcal{L}_{11} &= (\mathcal{D}^2 - k^2)^{-1}\left[k_y U_{\alpha Y}(\mathcal{D}^2 - k^2) - k_y U''_{\alpha Y} - \frac{1}{iRe_\alpha}(\mathcal{D}^2 - k^2)^2\right], \\ \mathcal{L}_{12} &= \frac{2k_z}{q}(\mathcal{D}^2 - k^2)^{-1}, \\ \mathcal{L}_{21} &= -\left(U'_{\alpha Y} + \frac{2}{q}\right)k_z, \\ \mathcal{L}_{22} &= k_y U_{\alpha Y} - \frac{1}{iRe_\alpha}(\mathcal{D}^2 - k^2). \end{aligned} \tag{32}$$

Now the solution of the Equation (30) is given by

$$Q = \sum_{m=1}^{\infty} C_m Q_{\mathcal{X},m}(\mathcal{X}) \exp\{(-i\sigma_m t)\}, \tag{33}$$

where the index m corresponds to the combined Orr–Sommerfeld and Squire modes and $Q_{\mathcal{X},m}(x)$ satisfies the eigenvalue equation

$$\mathcal{L}Q_{\mathcal{X},m}(\mathcal{X}) = \sigma_m Q_{\mathcal{X},m}. \tag{34}$$

Here σ is a complex quantity, given by $\sigma = \sigma_r + i\sigma_i$. In this article, σ_r, σ_i and hence σ for different parameters and different flows are obtained numerically. The numerical method for discretization is described in Section 7.

It is well known that a Poiseuille flow is linearly unstable under two-dimensional perturbation with $k_y = 1.02$ and $k_z = 0$, and the critical Re is about 5772.22. However, for the same Re, this flow is stable under perturbation with $k_y = k_z = 1$. Nevertheless, in the presence of Keplerian rotation of the whole system, i.e., due to the effect of the Coriolis force in the local rotating box, the situation changes. Figure 3 shows the eigenspectra for a linearly perturbed Poiseuille flow in the rotating frame (while the small region under consideration is rotating) with $q = 1.5$ (Keplerian rotation) for $k_y = k_z = 1$ for different Re_α. Here we observe that while the flow is stable for $Re_\alpha = 100$ and 1000 with $k_y = k_z = 1$, it is unstable for $Re_\alpha = 10{,}000$. Figure 4 also depicts the eigenspectra for the same flow as in Figure 3, but for $Re_\alpha = 6000$ and 7000. This confirms that an instability arises between $Re_\alpha = 6000$ and 7000. The critical Re_α is around 6431.473. Figure 5 depicts a sample of velocity eigenfunction, which is given here for the most unstable mode corresponding to a Poiseuille flow for $Re_\alpha = 7000$, $k_y = k_z = 1$, and $q = 1.5$.

Depending on the localization of the eigenfunctions, the corresponding modes are named. If the eigenfunctions have their maxima around the center of the domain, the corresponding modes are called body modes. If the eigenfunctions are localized around the boundary, the corresponding modes are called wall modes. See Kersale et al. (2004) for details about these modes. From Figure 5, we see that the modes are body modes.

We have imposed no-slip boundary conditions to obtain all the eigenspectra corresponding to a Poiseuille flow in the presence of rotation. However, for different boundary conditions, the unstable nature of the flow does not disappear from the system. Xiong & Tao (2020) argued that with the change in

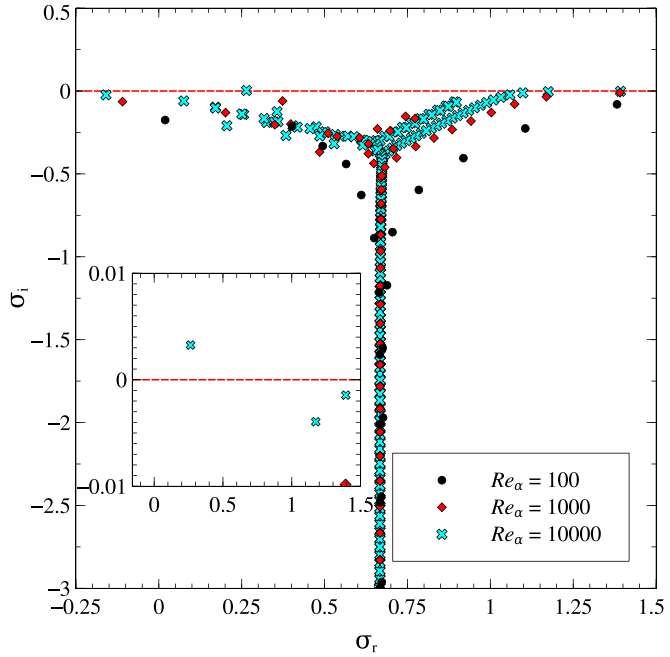

Figure 3. Eigenspectra for a linearized Poiseuille flow in the presence of Keplerian rotation ($q = 1.5$) of the box for $Re_\alpha = 100$, 1000, and 10,000, with $k_y = k_z = 1$.

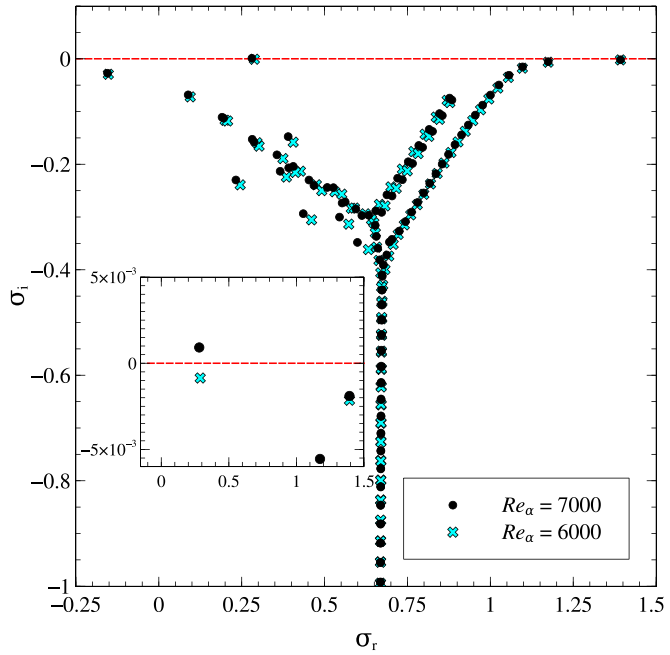

Figure 4. Same as Figure 3, but for $Re_\alpha = 6000$ and 7000.

boundary conditions, only the critical Reynolds number and other parameters, which reveal an instability, change.

To have a qualitative sense of why a plane Poiseuille flow in the presence of Keplerian rotation becomes unstable under three-dimensional perturbation unlike in the nonrotating case, below we investigate the effect of pure vertical perturbation.

5.2. Pure Vertical Perturbation

We consider pure vertical perturbation of the form u, $\zeta \sim u(t)$, $\zeta(t)\exp(ik_z z)$ for ease of analytical exploration, and

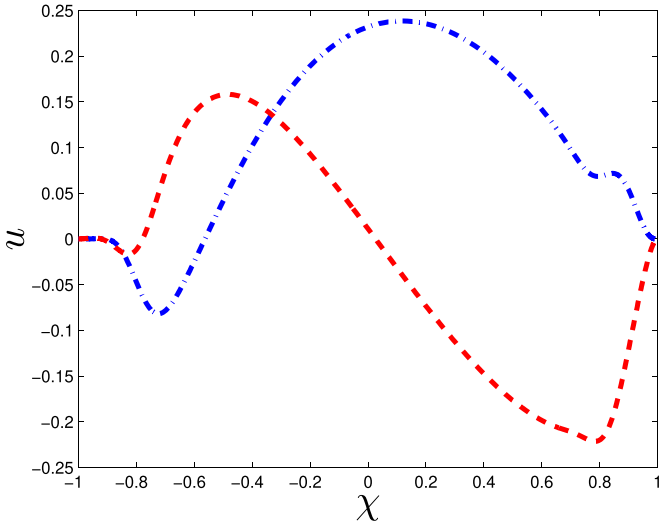

Figure 5. Velocity eigenfunction for the most unstable mode corresponding to a linearized Poiseuille flow in the presence of Keplerian rotation ($q = 1.5$) of the box for $Re_\alpha = 7000$ with $k_y = k_z = 1$. Dotted–dashed and dashed lines indicate the real and imaginary parts of u, respectively.

hence Equations (24) and (25) respectively reduce to

$$\frac{\partial u}{\partial t} - \frac{2i}{qk_z}\zeta = -\frac{1}{Re_\alpha}k_z^2 u \tag{35}$$

and

$$\frac{\partial \zeta}{\partial t} - ik_z\left(\frac{2}{q} + U'_{\alpha Y}\right)u = -\frac{1}{Re_\alpha}k_z^2\zeta. \tag{36}$$

Note, however, that this is just for the sake of an approximate analytical exploration, as due to shear in the x-direction, the perturbation cannot have this form, as we did not even choose it in our exploration of the eigenspectrum analysis. Combining Equations (35) and (36), we obtain a second-order temporal differential equation for $u(t)$, given by

$$\frac{\partial^2 u}{\partial t^2} + \frac{2k_z^2}{Re_\alpha}\frac{\partial u}{\partial t} + \left(\frac{4}{q^2} + \frac{2U'_{\alpha Y}}{q} + \frac{k_z^4}{Re_\alpha^2}\right)u = 0. \tag{37}$$

Let us consider the solution of Equation (37) to be $u(t) \sim \exp(\sigma t)$, $\gamma = 2k_z^2/Re_\alpha$ and $\beta = 4/q^2 + 2U'_{\alpha Y}/q + k_z^4/Re_\alpha^2$. Hence from Equation (37), we obtain a quadratic equation for σ, given by

$$\sigma^2 + \gamma\sigma + \beta = 0, \tag{38}$$

whose solution is

$$\sigma = -\frac{\gamma}{2} \pm \sqrt{-\frac{4}{q^2} - \frac{2U'_{\alpha Y}}{q}}. \tag{39}$$

If the background flow follows Equation (12), then Equation (39) becomes

$$\sigma = -\frac{\gamma}{2} \pm 2\sqrt{\frac{\mathcal{X}}{q} - \frac{1}{q^2}}. \tag{40}$$

From the above equation, it is clear that whenever the quantity under the root is real positive, one of the solutions for the vertical perturbation may grow with time exponentially. This depends on whether the magnitude of the term involved with

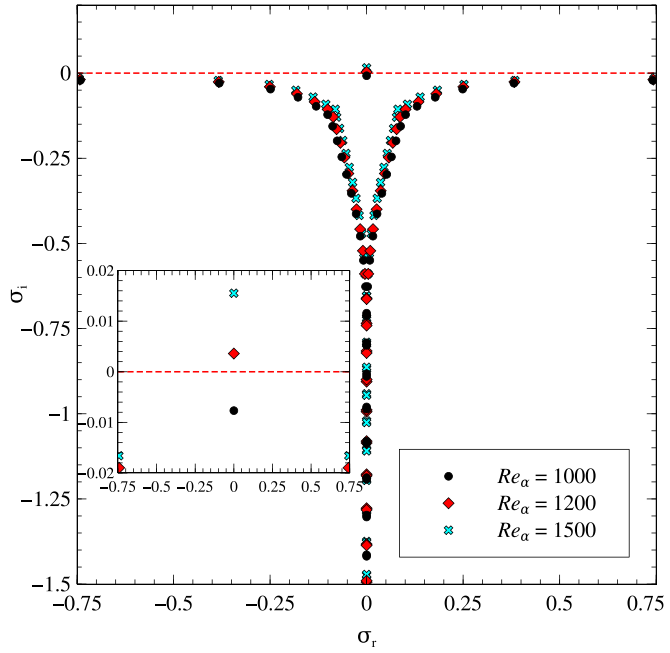

Figure 6. Eigenspectra for a linearized Poiseuille flow in the presence of Keplerian rotation ($q = 1.5$) of the box for $Re_\alpha = 1000$, 1200, and 1500, with a pure vertical perturbation, i.e., $k_y = 0$ and $k_z = 1$.

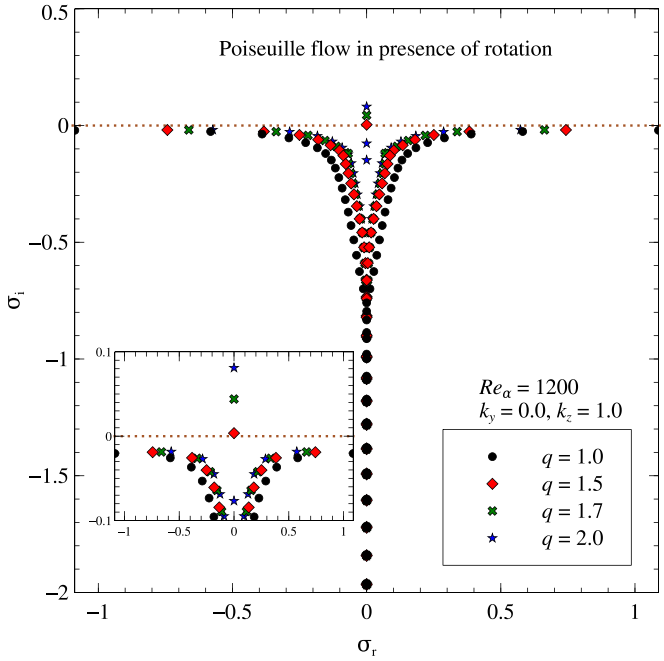

Figure 7. Eigenspectra of a linearized Poiseuille flow in the presence of rotation for vertical perturbation with $k_y = 0$ and $k_z = 1$ for four different q and $Re_\alpha = 1200$.

the square root (second term) is greater or smaller than the first term. As $\mathcal{X}$ varies between -1 and $+1$, it is very obvious that the vertical perturbation will grow for the system under consideration. However, as the growing modes correspond to a real positive σ_i, there is a lower bound of $\mathcal{X}$ for the modes to be confined in the system.

Figure 6 shows, by full numerical solutions, the eigenspectra for a Poiseuille flow in the presence of Keplerian rotation in the case of pure vertical perturbation, i.e., $k_y = 0$ and $k_z = 1$, for $Re_\alpha = 1000$, 1200, and 1500. From the inset, it is very clear that the flow is stable for $Re_\alpha = 1000$. However, it is unstable for $Re_\alpha = 1200$ and 1500, and the critical Re_α is around 1129.18.

These results argue that for an astrophysical accretion disk, when the flow is necessarily three-dimensional with rotation, a very small force makes the system unstable as its Re is huge (see, e.g., Mukhopadhyay 2013). Even if $\partial P/\partial Y$ vanishes, a finite $\Gamma_Y/\nu \equiv Re_\alpha \Gamma_Y$ would suffice for instability due to the emergence of a small contribution of x^2 (Poiseuille) effect along with an x (Couette) effect in the background. In fact, at large U_0, when the quadratic term in X in Equation (9) is small compared to the linear term in X, $Re_\alpha \to \nu U_0^3/2L^3\Gamma_Y^2$. Therefore a very small force Γ_Y along with a similarly small ν would render a huge Re_α, which might lead to linear instability and subsequent nonlinearity and turbulence in accretion disks. In a plane Couette flow in the laboratory, when ν is not very small, a small force would still lead to instability and turbulence at large U_0. For an intermediate U_0, the instability is expected to arise at an intermediate Re_α, as seen in experiments. The above arguments remain intact if the force is solely due to the unavoidable pressure gradient, whether tiny or not, such that $K = 1/(\nu\rho)\partial P/\partial Y$. We discuss in detail the relative importance of the external force and background velocity along with the viscosity in order to control the flow stability in Section 6 below.

5.3. Dependence of the Stability on the Rotation Profile

In the last two subsections, we have observed how the Keplerian rotation affects the three-dimensional and vertical perturbations. Here, we observe how the stability of a plane Poiseuille flow depends on the rotation profile, i.e., on different q. Figure 7 describes the eigenspectra of a Poiseuille flow for three different rotational profiles under a purely vertical perturbation. Here we note that for a fixed Re_α, larger q has a higher growth rate. In addition, we note that while $q = 1$ provides a stable flow, the other three chosen q result in unstable flow. For a three-dimensional perturbation (i.e., k_y and k_z are both nonzero) also, the stability decreases with increasing q, as is evident from Figure 8. However, as opposed to the purely vertical perturbation, in the three-dimensional case, flows of all q are stable for the chosen set of parameters.

Let us understand this fact from Equation (40). We consider two extreme cases of q, i.e., $q = 1$ and $q = 2$. Equation (40) for these two cases becomes

$$\sigma = -\frac{\gamma}{2} \pm 2\sqrt{\mathcal{X} - 1} \tag{41}$$

and

$$\sigma = -\frac{\gamma}{2} \pm \sqrt{2\mathcal{X} - 1}\,, \tag{42}$$

respectively. From Equation (41), we can obtain that the system will be unstable if $(\mathcal{X} - 1)$ is a positive real number and

$$\sqrt{\mathcal{X} - 1} > \frac{\gamma}{4} = \frac{k_z^2}{2Re_\alpha}. \tag{43}$$

Now, $(\mathcal{X} - 1)$ is negative other than at $\mathcal{X} = 1$ as $\mathcal{X} \in [-1, 1]$. However, at $\mathcal{X} = 1$, Equation (43) is not valid there either as $k^2/Re_\alpha > 0$ always. Therefore a plane Poiseuille flow with $q = 1$ will always be stable. This explains the reason behind the stable

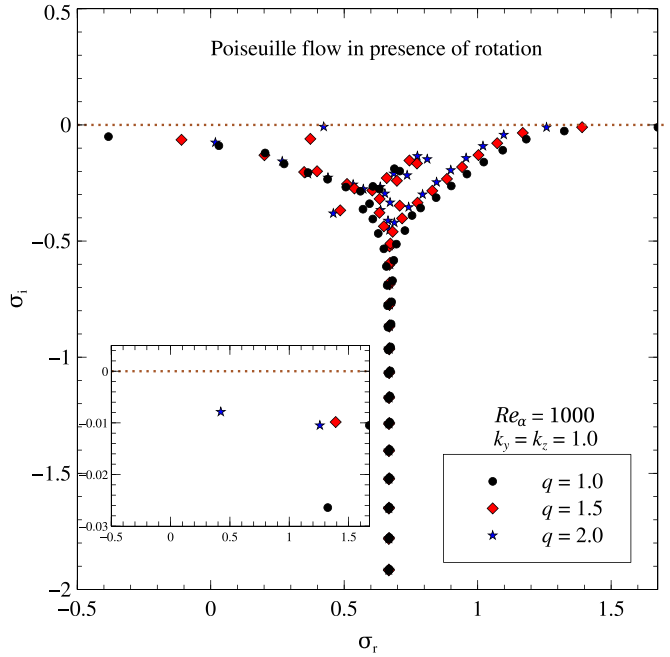

Figure 8. Eigenspectra of a linearized Poiseuille flow in the presence of rotation for three-dimensional perturbation with $k_y = k_z = 1$ for three different q and $Re_\alpha = 1000$.

Poiseuille flow with vertical perturbations for $q = 1$, as depicted in the Figure 7.

To make the system unstable for $q = 2$, from Equation (42), we require $(2\mathcal{X} - 1)$ to be a positive real number and

$$\sqrt{2\mathcal{X} - 1} > \frac{\gamma}{2} = \frac{k_z^2}{Re_\alpha}. \tag{44}$$

Now $(2\mathcal{X} - 1)$ could be positive within the domain of $\mathcal{X}$. Hence, for $q = 2$, a plane Poiseuille flow will be unstable depending on the parameters, i.e., k_z and Re_α.

Now for a general q (usually $1 \leqslant q \leqslant 2$ for the present interest), to make the system unstable, $\mathcal{X}/q - 1/q^2$ has to be a positive real number and also from Equation (40)

$$2\sqrt{\frac{\mathcal{X}}{q} - \frac{1}{q^2}} > \frac{\gamma}{2} = \frac{k_z^2}{Re_\alpha}. \tag{45}$$

It is important to check in which domain of $\mathcal{X}$, $\mathcal{X}/q - 1/q^2$ is positive and Equation (45) is satisfied. Moreover, it is also important to know how the maximum growth rates for vertical perturbations depend on q. The answers to these queries can be found in Figure 9, where the variation of $2\sqrt{\mathcal{X}/q - 1/q^2}$ as a function of $\mathcal{X}$ is shown for five different q. It shows that the size of the domain, in which $2\sqrt{\mathcal{X}/q - 1/q^2}$ remains a real number and hence $(\mathcal{X}/q - 1/q^2)$ remains a positive real number, decreases as q decreases. From Equation (40), it is obvious that the maximum growth rates will be higher for those q's for which $2\sqrt{\mathcal{X}/q - 1/q^2}$ will be larger. From Figure 9, we note that as q decrease, $2\sqrt{\mathcal{X}/q - 1/q^2}$ also decreases. This reveals that larger q will have higher growth rates with a larger domain. This explains the reason behind the higher growth rates (less stability) for vertical (three-dimensional) perturbations for larger q for a fixed Re_α.

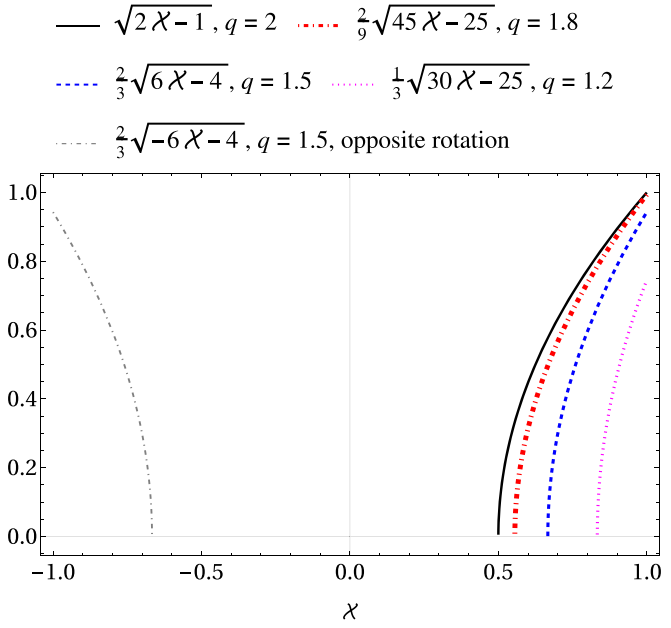

Figure 9. Variation of $2\sqrt{\mathcal{X}/q - 1/q^2}$ from Equation (40) as a function of $\mathcal{X}$ for $q = 1.2$, 1.5, 1.8, and 2.0 and for a oppositely rotating flow with $q = 1.5$.

Interestingly, the above findings argue for a striking similarities between the Papaloizou–Pringle instability (PPI; see e.g., Papaloizou & Pringle 1984; Balbus 2003) and the instability that we have obtained here, specifically, the one with the vertical perturbations. For PPI, the pressure gradient is nonzero in the equilibrium. In our case, we also consider a modified background due to the presence of a pressure gradient and/or an external force in the local frame. For PPI, the perturbations have to be nonaxisymmetric. These nonaxisymmetric perturbations contain the information of rotation (Balbus 2003). However, in our case, it is the vertical perturbation that couples with the rotation, playing an important role to reveal (faster) instability. Our vertical perturbation is therefore equivalent to the nonaxisymmetric perturbations required for PPI.

Now importantly, the sign of the terms involved with q (but not q itself) in the equations can be both positive and negative. The negative sign implies the opposite sense of rotation as compared to the positive sign. Figure 10 shows that the eigenspectra for a plane Poiseuille flow in the presence of rotation with either of the orientations for a vertical perturbation. We note that the eigenspectra are identical for both orientations of Keplerian rotation for a fixed Re_α. From Equation (40) and Figure 9, it is obvious that the negative rotational effect (when the term involved with $1/q$ is negative) is nullified by the negativity of $\mathcal{X}$, which is equivalent to the positive rotational effect in the positive $\mathcal{X}$ region. Hence, for the entire zone of $\mathcal{X}$, the net effect appears to be unchanged in either of the orientations of rotation. This explains why eigenspectra are independent of the orientation of rotation for a vertical perturbation. Nevertheless, for three-dimensional perturbation, this conclusion is also true. The reason is the following. In order to obtain the eigenspectra, we should have the secular determinant corresponding to the operator $\mathcal{L}$ in Equation (31). The information of rotation enters into the picture by $\mathcal{L}_{12}$ and $\mathcal{L}_{21}$. In this secular equation, $\mathcal{L}_{12}$ and $\mathcal{L}_{21}$ appear as a multiplication by themselves. More interestingly,

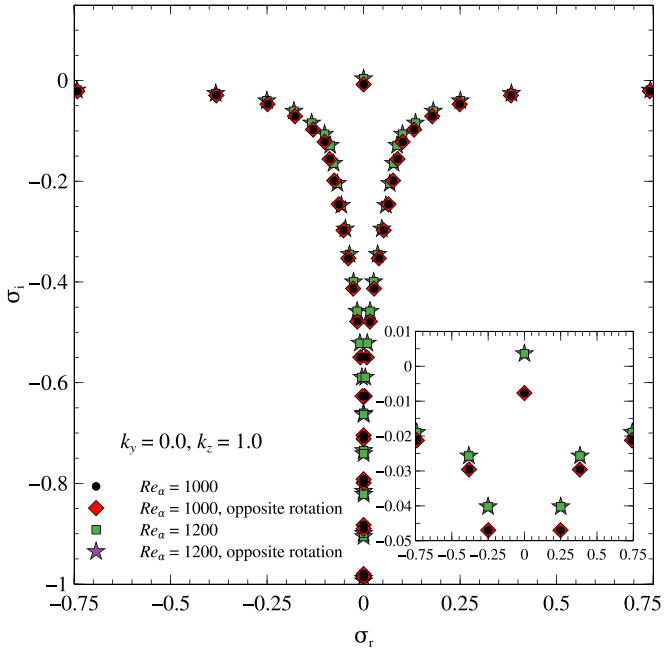

Figure 10. Eigenspectra of a linearized Poiseuille flow in the presence of rotation for vertical perturbation with $k_y = 0$, and $k_z = 1$ for Re_α, but for two opposite orientations of Keplerian rotation.

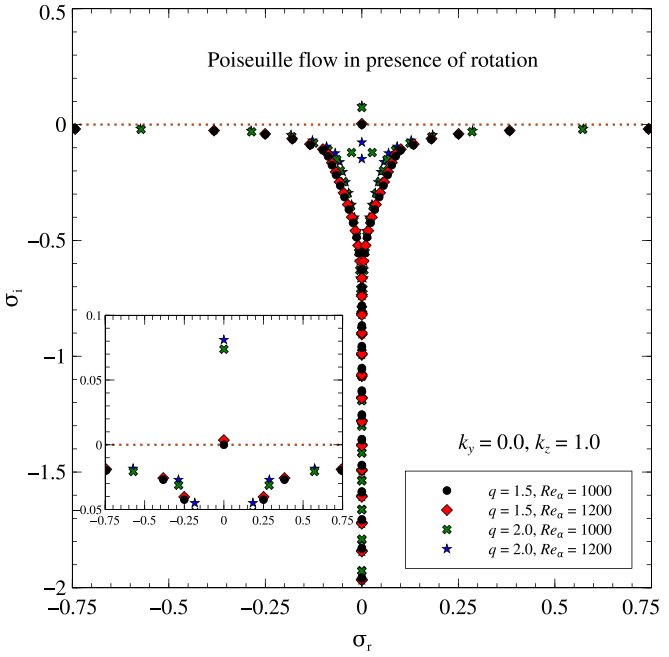

Figure 11. Eigenspectra of a linearized Poiseuille flow in the presence of rotation for vertical perturbation with $k_y = 0$, and $k_z = 1$ for two different q and Re_α.

we note that

$$\mathcal{L}_{12}\mathcal{L}_{21} = \left(\frac{\mathcal{X}}{q} - \frac{1}{q^2}\right)4k_z^2(\mathcal{D}^2 - k^2)^{-1}. \tag{46}$$

$\mathcal{L}_{12}\mathcal{L}_{21}$ therefore does not depend on the orientation of rotation because of the presence of $\mathcal{X}$, which spans from -1 to $+1$.

We can also obtain the domain of q that could give rise to an instability depending on other parameters. From Equation (40), the first condition for instability regardless of the orientation of rotation is

$$\frac{\mathcal{X}}{q} - \frac{1}{q^2} > 0, \tag{47}$$

or in other words,

$$\mathcal{X} > \frac{1}{q}. \tag{48}$$

For the flows with $q < 1$ (when q is positive for the present purpose), the above condition is violated. Hence, our primary domain of q for the plausible unstable flows in the present context is $q < \infty$, excluding the domain $q \in [0, 1]$. However, in the present context, the domain of interest is $q \in [1, 2]$ and $q \to \infty$ (conventional plane Couette flow without rotation).

Figure 11 describes the eigenspectra for a plane Poiseuille flow in the presence of rotation for a vertical perturbation to capture two phenomena. On one hand, it shows that for a fixed q, the increment of Re_α increases the growth rates of a vertical perturbation. On the other hand, it also depicts that the increment of q for a fixed Re_α increases the growth rates of a vertical perturbation. However, the latter has a stronger effect than the former. This is because when we observe the flow for a fixed q but at different Re_αs, we observe the same flow at different levels of initial velocity (lower Re_α corresponds to a more streamlined flow). However, for different qs, we study altogether different flows, when the stronger rotation is more prone to instability.

Figure 12 describes the variation in the maximum growth rate ($\sigma_{i,\max}$) as a function of q for vertical perturbation with $Re_\alpha = 1500$. Here the growth rates are maximized over the wavenumbers, k_z, i.e., we consider those k_zs that give rise to the maximum growth rate corresponding to each q. Figure 12 further shows that $\sigma_{i,\max}$ increases with increasing q, which can be understood qualitatively from Figure 9 and Equation (40).

Figure 13 describes eigenspectra of a plane Poiseuille flow in the presence of rotation for five different k_y. Interestingly, here we note that as k_y increases (i.e., the perturbation becomes more three-dimensional from purely vertical in nature), the flow becomes increasingly stabilized, or the unstable flow becomes stable. As we have already mentioned earlier, a plane Poiseuille flow becomes unstable at a $Re = 5772.22$ for planer (i.e., $k_z = 0.0$) perturbation. However, we have seen in the previous subsections and as we also discuss in Section 8 below, this rotational effect makes the flow unstable at a Re that is about two orders of magnitude lower than that obtained based on a planer perturbation. For a plane Poiseuille flow, the rotational effect (or the corresponding Coriolis effect) is therefore more likely to lead to instability than that from Tollmien–Schlichting waves (Alfredsson & Persson 1989), which are the corresponding planer perturbation modes at the critical Re. See Section 6.2 to understand other detailed physics behind the eigenspectra.

6. Perturbation Analysis of a Rotating Couette–Poiseuille Flow

6.1. The Formulation of a Dimensionless Background Flow

As shown in Section 2, a plane Couette flow in the presence of external force develops a nonlinear shear in addition to its background linear shear, as shown by Equation (9). This is called Couette–Poiseuille flow. Of course, in a suitable

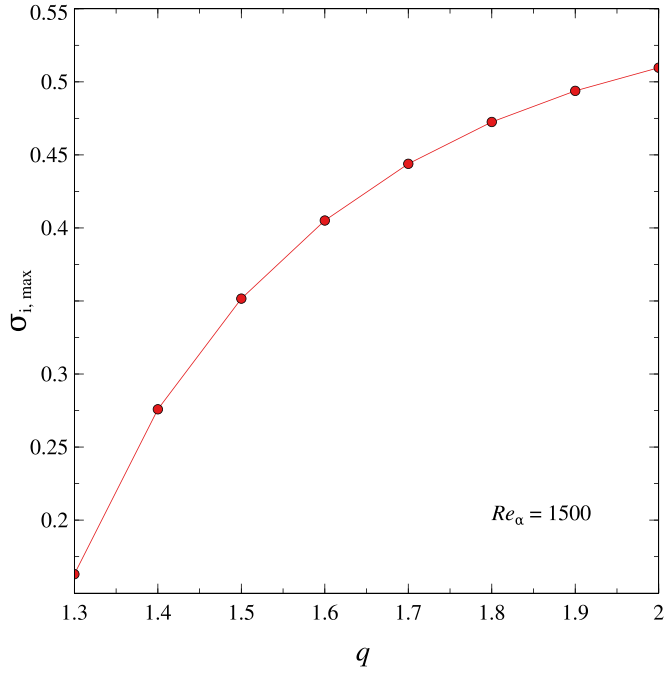

Figure 12. Maximum growth rate ($\sigma_{i,\max}$) as a function of q in a linearized Poiseuille flow for vertical perturbation with the k_z giving rise to $\sigma_{i,\max}$ for $Re_\alpha = 1500$.

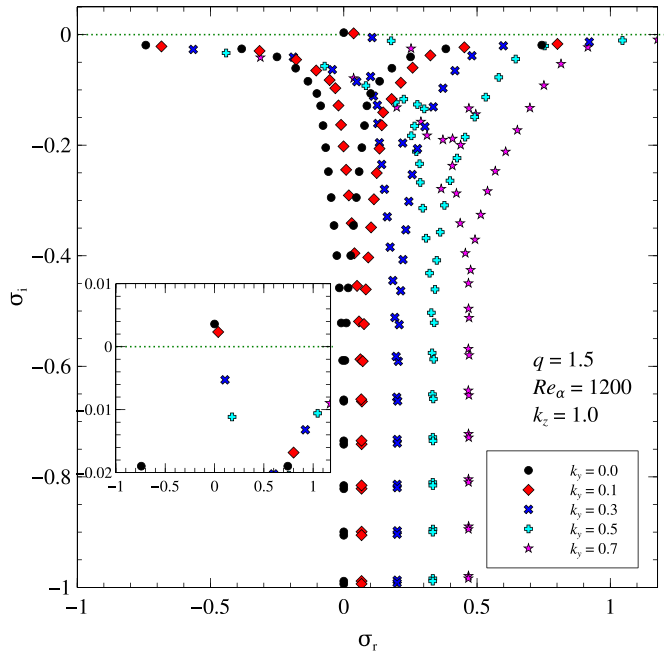

Figure 13. Eigenspectra of a linearized Poiseuille flow in the presence of Keplerian rotation for perturbations with $k_z = 1$, but with five different k_y for $Re_\alpha = 1200$.

coordinate frame, a plane Couette–Poiseuille flow will turn out to be a plane Poiseuille flow, as shown in Equation (10). Nevertheless, as shown by Figure 2, depending upon the flow parameters, i.e., strength of force and background velocity, the domain of a plane Poiseuille flow, more precisely, a plane Couette–Poiseuille flow, varies. This further affects the flow behavior under perturbation. Here, we explore a Couette–Poiseuille flow under various flow parameters. We therefore have to make Equation (9) dimensionless. In dimensionless units, Equation (9) turns out to be

$$U = \xi(1 - x^2) - x, \tag{49}$$

where $\xi = KL^2/2U_0 = \Gamma_Y L^2/2\nu U_0$ and $x = X/L$. The background velocity vector therefore is $\boldsymbol{U} = (0, U, 0)$.

To examine the stability of the background flow with velocity $\boldsymbol{U}$ within the domain, $x \in [-1, 1]$, in a rotating frame at R_0, we consider the same prescription of angular velocity of the rotating frame as chosen in Section 4.1, given by $\boldsymbol{\omega} = (0, 0, \Omega_0)$, $\Omega = \Omega_0(R/R_0)^{-q}$, and $\Omega_0 = U_0/qL$. Although a similar type of flow was explored by Balakumar (1997), they did not consider the effect of rotation, which is crucial for astrophysical bodies, in particular, for accretion disks. Following the same procedure as in Section 4.1, particularly from Equations (19) to (22), we can redefine the Reynolds number corresponding to the flow as

$$Re = \frac{U_0 L}{\nu}, \tag{50}$$

and $\boldsymbol{\Gamma}_{\rm cp} = \boldsymbol{\Gamma} L/U_0^2$. We can also rewrite ξ as

$$\xi = \Gamma_Y Re L/2U_0^2. \tag{51}$$

6.2. The Perturbation Analysis

To perform a perturbation analysis for the background flow described by Equation (49), we follow the same procedure as described in Section 4.2 and obtain the corresponding Orr–Sommerfeld and Squire equations similar to Equations (24) and (25), given by

$$\left(\frac{\partial}{\partial t} + U\frac{\partial}{\partial y}\right)\nabla^2 u - U''\frac{\partial u}{\partial y} + \frac{2}{q}\frac{\partial \zeta}{\partial z} - \frac{1}{Re}\nabla^4 u = 0, \tag{52}$$

and

$$\left(\frac{\partial}{\partial t} + U\frac{\partial}{\partial y}\right)\zeta - U'\frac{\partial u}{\partial z} - \frac{2}{q}\frac{\partial u}{\partial z} - \frac{1}{Re}\nabla^2 \zeta = 0, \tag{53}$$

where the prime denotes differentiation with respect to x. The corresponding no-slip boundary conditions are $u = v = w = 0$ at the two boundaries $x = \pm 1$, or equivalently, $u = \frac{\partial u}{\partial x} = \zeta = 0$ at $x = \pm 1$ (see Mukhopadhyay et al. 2005; Ghosh & Mukhopadhyay 2021). We then substitute solution forms given by Equations (26) and (27), but replacing $\mathcal{X}$ by x, in Equations (52) and (53), and eventually obtain Equation (30) through Equations (28) and (29), where $\mathcal{L}$ and the elements of $\mathcal{L}$ are given by Equations (31) and (32), but replacing U_α, Re_α, and $\mathcal{D} = \partial/\partial\mathcal{X}$ by U, Re, and $\mathcal{D} = \partial/\partial x$, respectively.

To have a qualitative idea about the eigenspectra, the analytical exploration based on pure vertical perturbations, shown in Section 5.2 for a plane Poiseuille flow, is of great use. Replacing $U'_{\alpha Y}$ by U' in Equation (39) for a Couette–Poiseuille flow, the growth rate turns out to be

$$\sigma_{\rm CP} = -\frac{\gamma_{\rm CP}}{2} \pm \sqrt{-\frac{4}{q^2} + \frac{4\xi x}{q} + \frac{2}{q}}, \tag{54}$$

where $\gamma_{CP} = 2k_z^2/Re$. For the marginal instability, the discriminant in Equation (54) becomes zero, and hence

$$q = \frac{2}{2\xi x + 1}. \tag{55}$$

If we consider $\xi = 0$ in Equation (55), we see that a marginal instability occurs at $q = 2$. However, for the concerned flow, this condition is relaxed by the presence of ξ. The constraint on q can be drawn from the domain size, i.e., $|x| \leqslant 1$. The restrictions on q for marginal instability are therefore

$$q > \frac{2}{2\xi + 1} \text{ for } x < 1, \tag{56}$$

and

$$q < \frac{2}{1 - 2\xi} \text{ for } x > -1. \tag{57}$$

Similarly, we can obtain the constraint on ξ as well. To have the instability, the discriminant in Equation (54) has to follow the condition given by

$$-\frac{4}{q^2} + \frac{4\xi x}{q} + \frac{2}{q} \geqslant 0, \tag{58}$$

and hence $\xi x \geqslant 1/q - 1/2$. The constraint on ξ is therefore given by

$$\xi > \frac{1}{q} - \frac{1}{2}. \tag{59}$$

For a Keplerian flow, i.e., $q = 1.5$, $\xi > 0.167$.

Figure 14, however, describes the exact eigenspectra for a Couette–Poiseuille flow in the presence of Keplerian rotation ($q = 1.5$) for vertical perturbation with $k_y = 0$ and $k_z = 1$ for several ξ and Re. As the figure shows, for $\xi = 0.3$, the system is unstable, while for $\xi = 0.15$ and 0.17, the system is stable. This is to recall that the apparent discrepancy between the results based on Equation (59) and Figure 14 is due the inexact nature of the eigenvalue given by Equation (54). Equation (54) corresponds to a qualitative description of the vertical perturbation for a Couette–Poiseuille flow. While deriving Equation (54), we have considered the perturbation to be the function of z only. However, in reality, in order to obtain the eigenvalues (here for vertical perturbation), the perturbation has to be the function of both x and z, as indeed was considered in order to obtain eigenspectra shown in Figure 14. This leads to a differential equation of x, which we solve with the no-slip boundary condition to have the eigenspectra. Hence, while Equation (54) and the conditions derived from it give a qualitative idea for the eigenspectra, they do not provide an exact information. In Figure 14, we also note that for $\xi = 0.3$, the system is more unstable for $Re = 2000$ than for $Re = 1500$. It is quite easy to understand from Equation (54) that keeping the other parameters, i.e., q, ξ, and k_z, fixed, if we increase Re, γ_{CP} decreases, and hence σ_{CP} increases.

Figures 15 and 16 describe the eigenspectra for a Couette–Poiseuille flow in the presence of rotation with different rotation parameters for vertical and three-dimensional perturbations, respectively. For both cases, we see that as the rotation parameter increases, the system becomes more unstable. If there is no rotation in the system, it is stable for the parameters considered in these two cases. Figure 17 depicts an example for

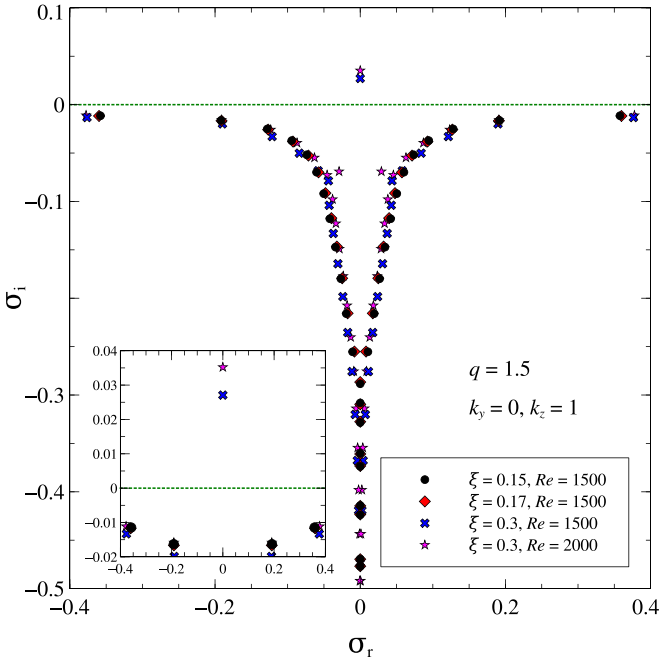

Figure 14. Eigenspectra for a Couette–Poiseuille flow, described by Equation (49), in the presence of Keplerian rotation ($q = 1.5$) for vertical perturbation with $k_y = 0$ and $k_z = 1$ for different Re and ξ.

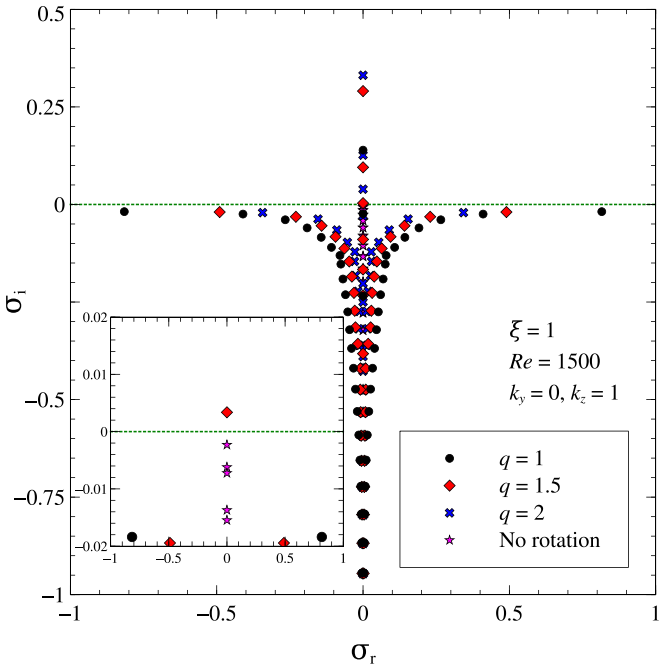

Figure 15. Eigenspectra for a Couette–Poiseuille flow, described by Equation (49), in the presence of rotation for vertical perturbation with $k_y = 0$ and $k_z = 1$ for different rotation parameters (q), $Re = 1500$ and $\xi = 1$.

the nature of the velocity eigenfunction, which is given for the most unstable mode corresponding to a Couette–Poiseuille flow with $Re = 3000$, $k_y = 0.5$, $k_z = 1$, and $q = 1.5$. According to Kersale et al. (2004), these are body modes.

Figures 18 and 19 describe the eigenspectra for a Couette–Poiseuille flow in the presence of rotation for vertical and three-dimensional perturbations, respectively, for different ξ. For both cases, we note that as ξ increases, the system becomes

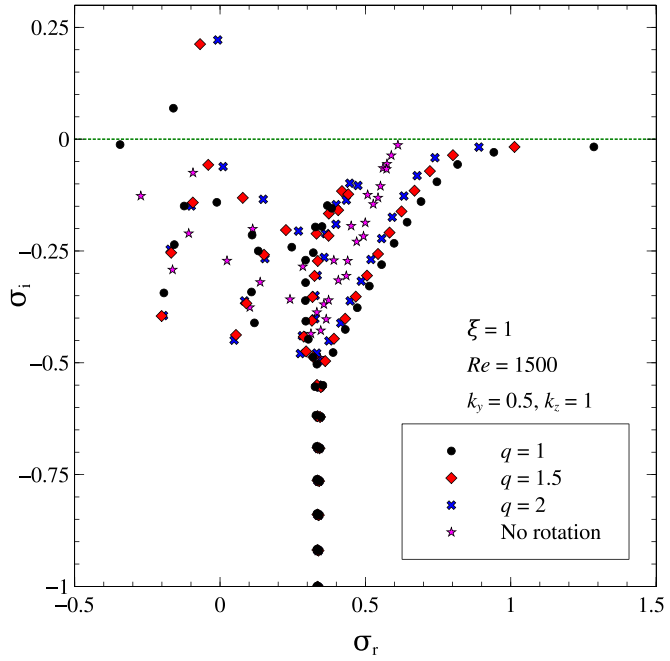

Figure 16. Eigenspectra for a Couette–Poiseuille flow, described by Equation (49), in the presence of rotation for three-dimensional perturbation with $k_y = 0.5$ and $k_z = 1$ for different rotation parameters (q), $Re = 1500$ and $\xi = 1$.

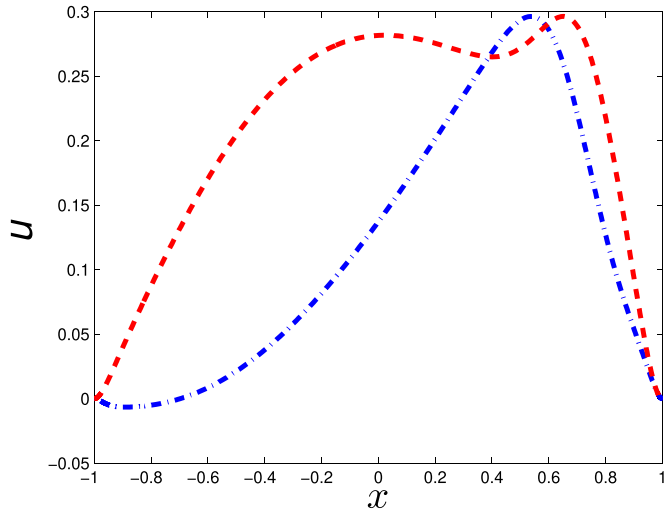

Figure 17. Velocity eigenfunction for the most unstable mode corresponding to a linearized Couette–Poiseuille flow in the presence of Keplerian rotation ($q = 1.5$) of the box for $Re = 3000$ with $k_y = 0.5$ and $k_z = 1$. Dotted–dashed and dashed lines indicate the real and imaginary parts of u, respectively.

more unstable. From Equation (54), we can qualitatively explain this behavior. The discriminant in Equation (54) and hence σ_{CP} increase as ξ increases for a fixed q.

Figure 20 describes the eigenspectra for a Couette–Poiseuille flow in the presence of Keplerian rotation for for $k_y = 1$ and various k_z. We note that as k_z increases and other parameters are kept fixed, the system becomes more unstable. From Equation (32), it is clear that rotation (i.e., q) is coupled with k_z and the shear velocity is coupled with k_y. As k_z increases, the effect of rotation in the system therefore dominates the effect of shear. It is now quite evident from the whole discussion that rotation and shear have opposite effects on the stability of the

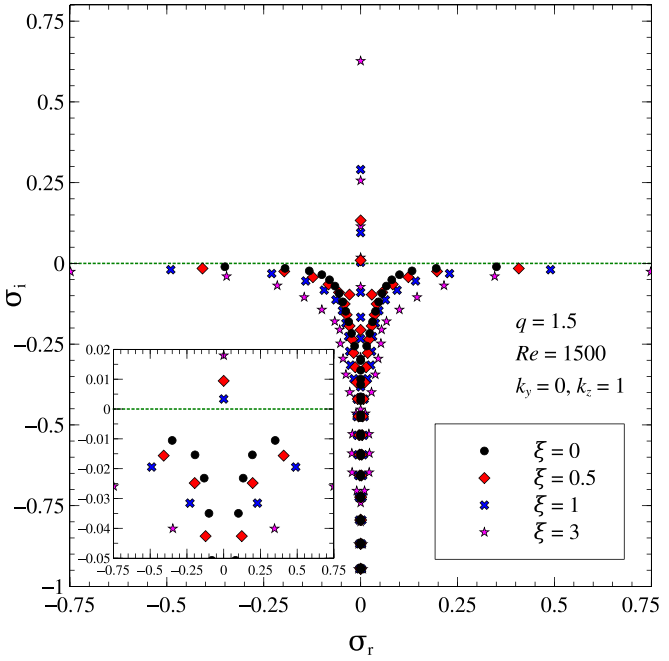

Figure 18. Eigenspectra for a Couette–Poiseuille flow, described by Equation (49), in the presence of Keplerian rotation ($q = 1.5$) for vertical perturbation with $k_y = 0$ and $k_z = 1$, $Re = 1500$ and different ξ.

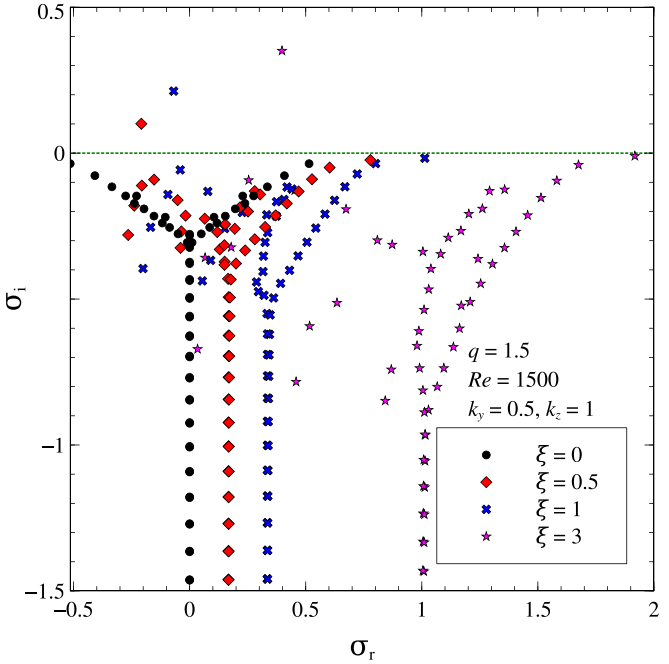

Figure 19. Eigenspectra for a Couette–Poiseuille flow, described by Equation (49), in the presence of Keplerian rotation ($q = 1.5$) for three-dimensional perturbation with $k_y = 0.5$ and $k_z = 1$, $Re = 1500$ and different ξ.

flow. Rotation tries to make the flow more unstable, while shear tries to stabilize it. This is also clearly described in Figure 21. The figure describes the eigenspectra for a Couette–Poiseuille flow in the presence of Keplerian rotation for $k_z = 1$ and various k_y. As k_y increases, the flow becomes more dominated by shear than rotation which causes the flow to become more stable.

Interestingly, Figures 13, 19 and 21 show that the entire eigenspectrum keeps shifting to the positive σ_r direction with

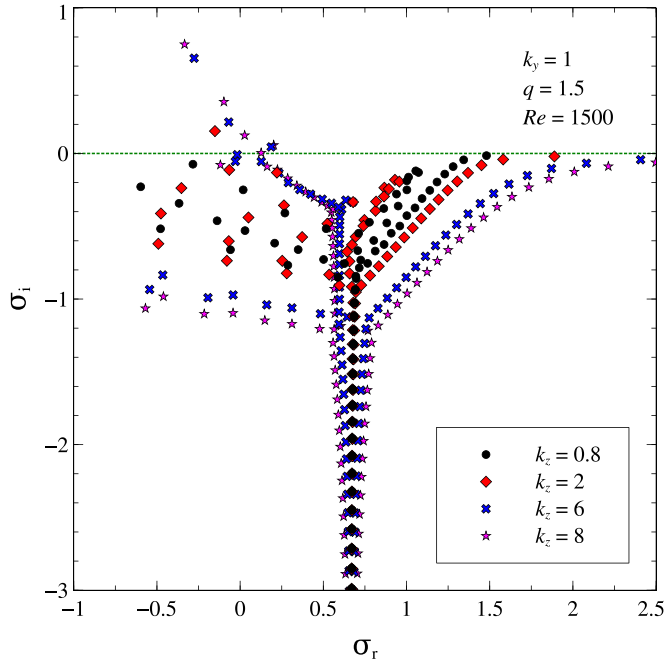

Figure 20. Eigenspectra for a Couette–Poiseuille flow, described by Equation (49), in the presence of Keplerian rotation ($q = 1.5$) for $k_y = 1$, different k_z, $Re = 1500$ and $\xi = 1$.

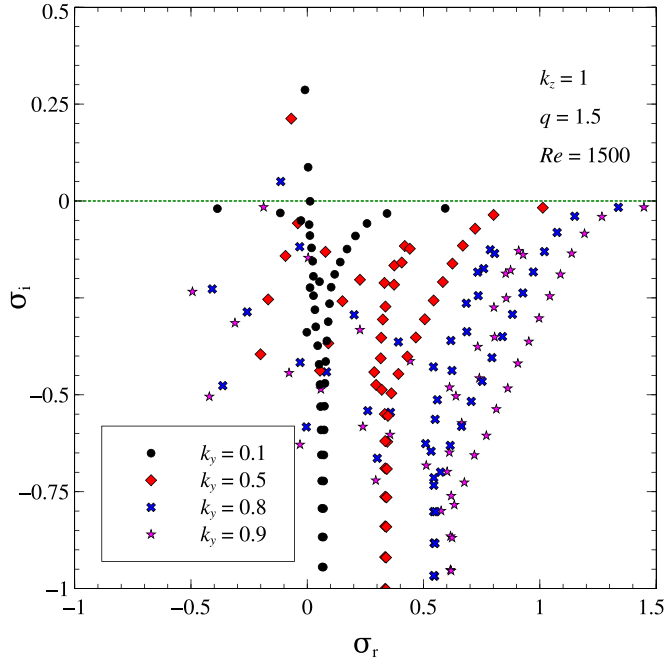

Figure 21. Eigenspectra for a Couette–Poiseuille flow, described by Equation (49), in the presence of Keplerian rotation ($q = 1.5$) for different k_y, $k_z = 1$, $Re = 1500$ and $\xi = 1$.

increasing k_y or ξ. This can be qualitatively understood in the following analysis. Assuming that approximate solutions for Equations (52) and (53) are $u, \zeta \sim \exp(\sigma_{\rm CP3} t + \tilde{\boldsymbol{k}} \cdot \boldsymbol{r})$, where $\tilde{\boldsymbol{k}} \equiv (k_x, k_y, k_z)$ and $\boldsymbol{r} \equiv (x, y, z)$, we obtain

$$\sigma_r = \left(U + \frac{U''}{2\tilde{k}^2}\right) k_y \pm f(k_x, k_y, k_z, U', U'', q), \qquad (60)$$

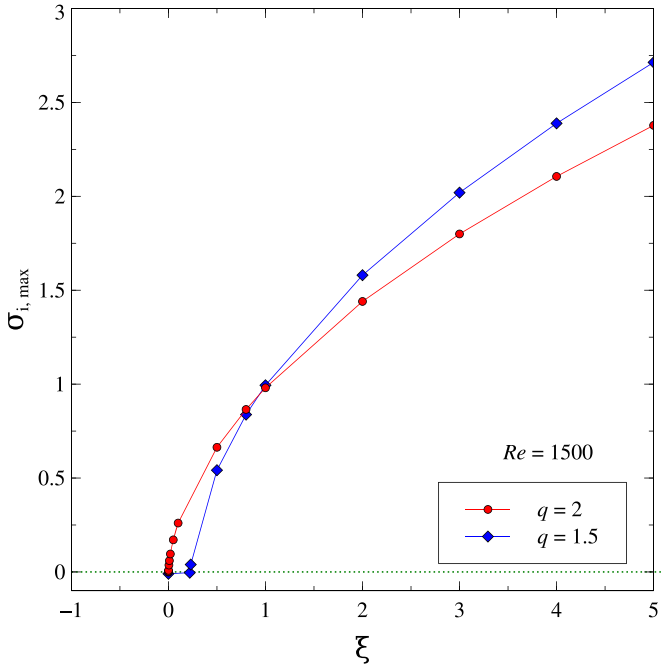

Figure 22. Maximum growth rate ($\sigma_{i,\max}$) as a function of ξ for a Couette–Poiseuille flow with $q = 1.5$, 2.0 having vertical perturbation for k_z maximizing $\sigma_{i,\max}$ and $Re = 1500$.

where the function $f(k_x, k_y, k_z, U', U'', q)$ is determined by the natures of background flow, perturbation, and rotation, $\sigma_{\rm CP3} = \sigma_i - i\sigma_r$, according to our convention of the original exact solution given by Equation (33) and eigenspectra. Note, however, that the solution in the x-direction in principle should not be of the plane waveform as U is a function of x, which indeed we do not choose in order to compute the eigenspectra. It is easy to check that the magnitude of $f(k_x, k_y, k_z, U', U'', q)$ is smaller than the first term in parentheses in Equation (60), and σ_r increases with increasing k_y for the background flows and generally for the parameters considered here. Therefore Equation (60) confirms that as k_y increases, σ_r increases, with a shift in the positive σ_r direction, as seen in Figures 13 and 21. Similarly, with increasing ξ, the Couette–Poiseuille flow tends to become a pure Poiseuille flow and $\sigma_r \to (1 - x^2 - 1/\tilde{k}^2)\xi k_y$. Therefore ξ and k_y play interchangeable roles, and hence, with increasing ξ, σ_r increases, as seen in Figure 19.

Figure 22 describes the maximum growth rate ($\sigma_{i,\max}$) as a function of ξ for a Couette–Poiseuille flow having a vertical perturbation with k_z maximizing σ_i. It shows that $\sigma_{i,\max}$ increases monotonically with ξ for both qs. It also shows that if $\xi \lesssim 1$, $\sigma_{i,\max}$ for $q = 2$ is larger than that for $q = 1.5$. However, the situation reverses for $\xi > 1$. This phenomenon can be understood qualitatively from Figure 23, where we show the variation of $\sqrt{-4/q^2 + 4\xi x/q + 2/q}$ from Equation (54) as a function of x for several combinations of q and ξ. We see that for $\xi = 0.5$, $\sqrt{-4/q^2 + 4\xi x/q + 2/q}$ is larger for $q = 2$ than for $q = 1.5$. As a result, $\sigma_{\rm CP}$ in Equation (54) becomes larger for $q = 2$ than for $q = 1.5$. This explains the behavior of $\sigma_{i,\max}$ for $\xi \lesssim 1$ in Figure 22. Similarly, the explanation of larger $\sigma_{i,\max}$ for $\xi > 1$ in Figure 22 can be extracted from the curves with $q = 1.5$ and $q = 2$ at $\xi = 5.0$ in Figure 23. It is further verified from Figure 22 that below a certain ξ, depending on q, the flow becomes stable with negative $\sigma_{i,\max}$.

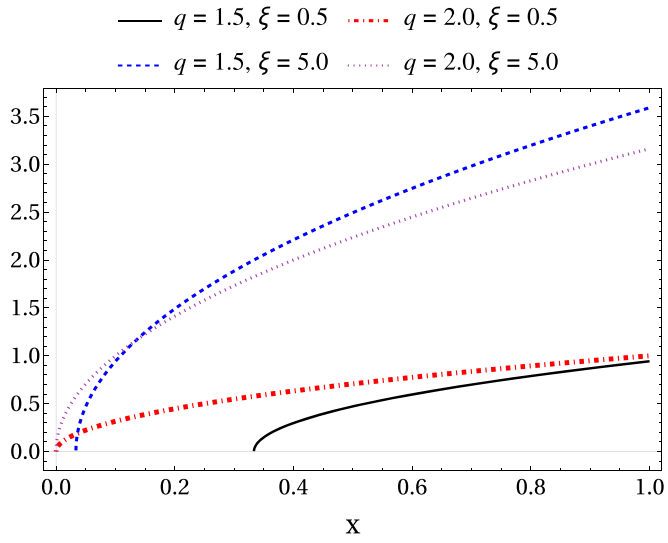

Figure 23. Variation of $\sqrt{-4/q^2 + 4\xi x/q + 2/q}$ from Equation (54) as a function of x for several combinations of q and ξ.

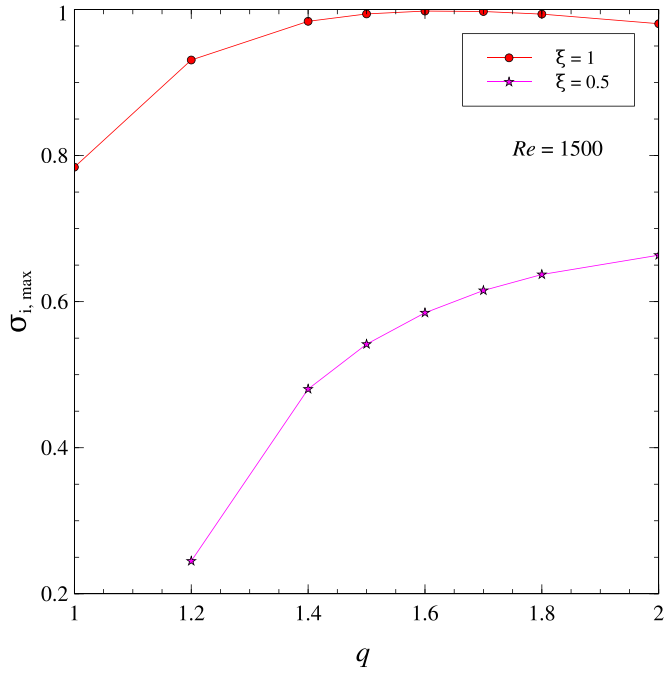

Figure 24. Maximum growth rate ($\sigma_{i,\max}$) as a function of q for a Couette–Poiseuille flow with $\xi = 0.5$, 1.0 having vertical perturbation for k_z maximizing $\sigma_{i,\max}$ and $Re = 1500$.

Figure 24 describes the maximum growth rate as a function of q for a Couette–Poiseuille flow with $\xi = 0.5$, 1.0 and $Re = 1500$ for vertical perturbation with k_z maximizing σ_i. It shows that $\sigma_{i,\max}$ increases with increasing q for $\xi = 0.5$. However, for $\xi = 1$, $\sigma_{i,\max}$ increases with increasing q only up to $q \sim 1.6$, subsequently, it decreases. This behavior can be qualitatively understood from Figure 25, where we show the variation of the discriminant in the Equation (54) as a function of x with $\xi = 1$ and for $q = 1.0$, 1.4, 1.6, 1.8, and 2.0. It shows that the case of $q = 1.4$ gives rise to the maximum discriminant. However, the maximum discriminants for $q = 1$ and 2 are almost the same, and they are the least of all the qs. Hence $\sigma_{\rm CP}$ from Equation (54) will be the highest for $q = 1.4$ and lowest for $q = 1$ and 2. This qualitative analysis therefore indicates

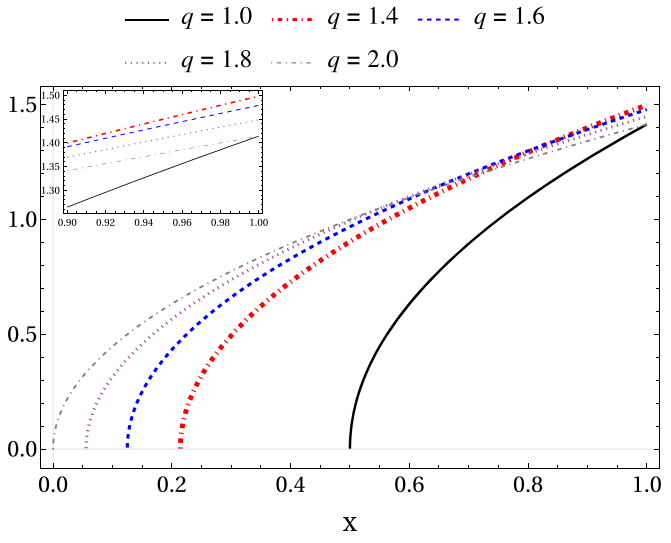

Figure 25. Variation of $\sqrt{-4/q^2 + 4\xi x/q + 2/q}$ from Equation (54) as a function of x for $\xi = 1$ and for several q's.

that $\sigma_{i,\max}$ is not expected to increase with the increase of q throughout at any ξ.

6.3. Viable Magnitude of Force

From the bound on ξ for a Keplerian flow described above, we can estimate the extra force, Γ_Y. From Equation (51), we have

$$U_0 = \sqrt{\frac{\Gamma_Y L Re}{2\xi}}. \tag{61}$$

The size of the shearing box, L, is $0.05R_s$ (Nath & Mukhopadhyay 2015), where $R_s = 2GM/c^2$ is the Schwarzschild radius for the central black hole of mass M, with G and c the gravitational constant and speed of light in free space, respectively. From Mukhopadhyay (2013), we obtain that for accretion disk, $Re \gtrsim 10^{14}$. Considering all these and the lowest bound on ξ, i.e., $\xi = 0.167$ for a Keplerian disk, we obtain

$$U_0 = \sqrt{5\overline{m}\ \overline{n}\ \Gamma_Y} \times 10^9 \text{ cm sec}^{-1} \simeq \sqrt{\overline{m}\ \overline{n}\ \Gamma_Y}\frac{c}{10}, \tag{62}$$

where $Re = \overline{n}10^{14}$, $M = \overline{m}M_\odot$ and $M_\odot$ is the mass of the Sun. Now at a radius R, the speed would be

$$U_0 = \sqrt{\frac{GM}{R}} = \frac{c}{\sqrt{2\rho}}, \tag{63}$$

where $R = \rho R_s$. If the fluid is at 100 R_s, then $U_0 = c/10\sqrt{2}$. From Equations (62) and (63), we obtain $\Gamma_Y = 0.5/\overline{m}\ \overline{n}$ cm sec^{-2}. This confirms that the extra force is indeed very small for the accretion disk around an astrophysical black hole whose Re is huge. For example, a supermassive black hole of mass $10^7 M_\odot$ having an accretion disk with $Re = 10^{22}$ leads to $\Gamma_Y = 5 \times 10^{-16}$ cm sec^{-2}, which is too small compared to the acceleration due to the gravity of the black hole at that position. This confirms that indeed a tiny Γ_Y, i.e., a very small effect of external force, would make the flow unstable.

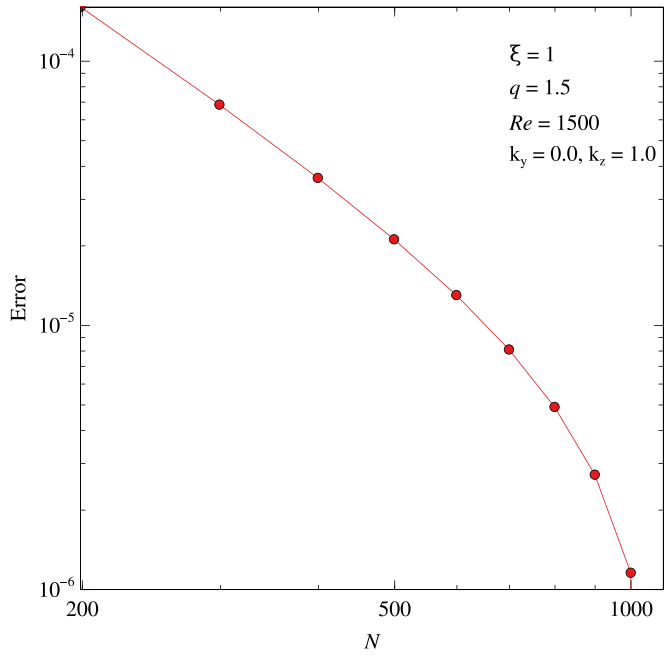

Figure 26. Error as a function of N for a Couette–Poiseuille flow with $\xi = 1$, $q = 1.5$, $Re = 1500$, $k_y = 0$, and $k_z = 1.0$.

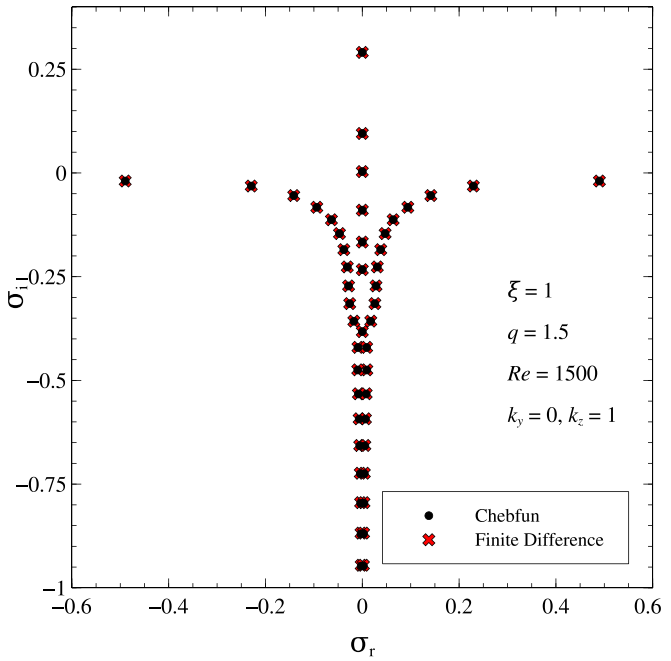

Figure 27. Eigenspectra for a Couette–Poiseuille flow with $\xi = 1$ in the presence of Keplerian rotation for $Re = 1500$, $k_y = 0$, and $k_z = 1$, obtained using Chebfun and finite-difference methods.

7. Accuracy of Numerics

Throughout the work, we have used the finite-difference method to obtain the eigenspectra. We particularly have used the second-order central difference method. Equation (34) is an eigenvalue equation, which is the function x. To solve it numerically, we discretize the domain that ranges from $x = x_0 = -1$ to $x = x_f = 1$. In our calculation, we have divided the domain into $(N + 1)$ segments, where the width of the each segment is defined as

$$h = \frac{x_f - x_0}{N + 1}. \tag{64}$$

For all the eigenspectra presented in this work, $N = 499$. Therefore the dimension of $\mathcal{L}$ in Equation (34) after using the finite-difference method is $2N \times 2N$. To check the accuracy and the convergence of the eigenvalues for the chosen matrix dimension, we show the variation of the error $= \sigma_{i,\max}(N) - \sigma_{i,\max}(N = 1099)$ as a function of N in Figure 26 for a typical set of parameters. It confirms that the chosen $N = 499$ leads to the optimum numerical values of σ_i, which hardly changes with further increasing N. In fact, the variation of $\sigma_{i,\max}$ for $199 \leqslant N \leqslant 1099$ is not more than $\sim 10^{-4}$.

However, to check the accuracy of the eigenspectra, particularly the most unstable modes as these are the most important feature of this work, we have also verified the result of the finite-difference method with those obtained using Chebfun (Driscoll et al. 2014). Figure 27 demonstrates the eigenspectra for a Couette–Poiseuille flow for a given set of parameters. It confirms that the two eigenspectra match each other quite well, which confirms the accuracy of our results.

8. Discussion

In the previous sections, we have observed that the stability of a rotating Poiseuille flow and a Couette–Poiseuille flow

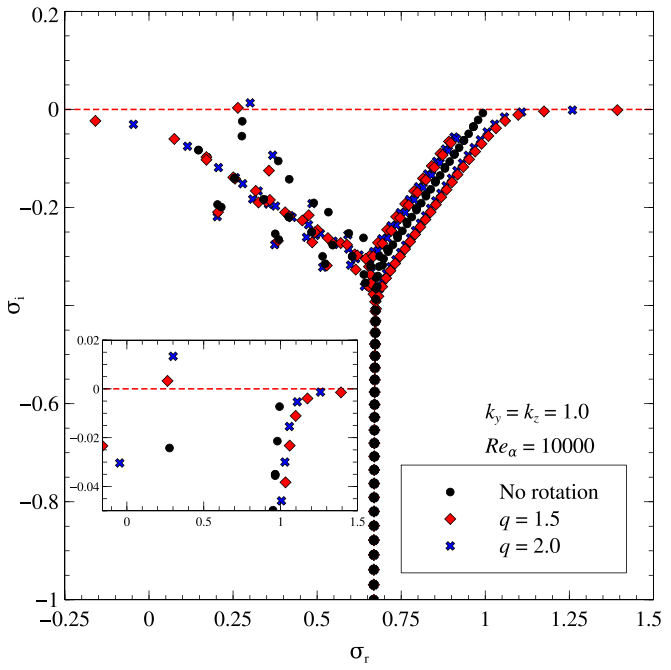

Figure 28. Eigenspectra of a linearized Poiseuille flow in the presence of rotation for three-dimensional perturbation with $k_y = k_z = 1$ for three different q and Re_α=10,000.

greatly depends on q and also on the nature of perturbation. To make this statement more concrete, we show in Figure 28 the eigenspectra of a plane Poiseuille flow in the presence and absence of rotation for a three-dimensional perturbation with $k_y = k_z = 1$. Here, we note that the Poiseuille flow is stable even for $Re_\alpha = 10{,}000$ with $k_y = k_z = 1$, when rotational effect has not been taken into account. In contrast, when rotation is there, the flow becomes unstable, and as q increases, the maximum growth rate increases for the same set of other parameters. We therefore argue that rotation makes the plane Poiseuille flow

Table 1
Critical Values of the Reynolds Number ($Re_{\alpha,\mathrm{cric}}$) and Critical Values of k_z ($k_{z,\mathrm{cric}}$) for Three Different Rotation Parameters, q, for a Plane Poiseuille Flow in the Presence of Rotation for Vertical Perturbation, i.e., $k_y = 0$

q	$Re_{\alpha,\mathrm{cric}}$	$k_{z,\mathrm{cric}}$
2.0	137.2969	4.066
1.8	174.84	4.5762
1.5	327.58	6.1

unstable. On the other hand, rotation has an opposite effect on a plane Couette flow. This is clear from Equation (39) by substituting $U_{\alpha Y} = -\mathcal{X}$ and hence $U'_{\alpha Y} = -1$. Equation (39) then becomes

$$\sigma = -\frac{\gamma}{2} \pm \frac{\sqrt{2}}{q}\sqrt{q-2}, \tag{65}$$

and hence

$$\sigma = -\frac{\gamma}{2} \pm \frac{i}{\Omega q}\kappa, \tag{66}$$

where κ is the epicyclic frequency, given by $\kappa = \Omega\sqrt{2(2-q)}$. Now for $q < 2$, κ is always a positive real number, and hence, a plane Couette flow with a rotational effect is always stable as long as $q < 2$. On the other hand, Equation (40) shows that even if $q < 2$, a plane Poiseuille flow with rotation becomes unstable in a particular domain of flow depending on q.

In Section 5.3 we have argued that as q increases for a fixed Re_α, the maximum growth rates increases. This statement matches results in the literature well, i.e., Lezius & Johnston (1976; their Figure 2) and Alfredsson & Persson (1989). However, these authors considered "*Ro*" as the rotation parameter, and it is inverse of q. In addition, the background flow considered by them is $6(\mathcal{X} - \mathcal{X}^2)$. This is the reason behind the different critical *Re* and wavevector in the present work compared to Lezius & Johnston (1976) and Finlay (1990; see their Table 1). While they obtained a critical $Re \sim 89$ and a critical wavevector ~ 5, we have obtained them as 137.2969 and 4.066, respectively, for the vertical perturbation and $q = 2$, e.g., as provided in Table 1, which lists the critical *Re* ($Re_{\alpha,\mathrm{cric}}$) and the critical wavevector ($k_{z,\mathrm{cric}}$) for different rotation parameters. We note that $Re_{\alpha,\mathrm{cric}}$ increases as q decreases, as expected from the whole discussion.

Note importantly that the inclusion of rotation does not invalidate the Squire theorem, which states that a flow that is unstable in three dimensions will be unstable in two dimensions at a lower *Re*. This is obvious from Figures 13 and 21. As k_y is nonzero and increases further, keeping other parameters fixed, we see that the growth rate of the most unstable mode or least stable mode decreases.

9. Conclusion

In the presence of extra force, a plane Couette flow behaves more like a plane Poiseuille flow. However, depending on the strength of force and the boundary conditions, it may almost behave like a plane Couette flow, or the deviation from plane Couette flow may be small. Nevertheless, when this flow is studied in the presence of the Coriolis effect, it becomes unstable under three-dimensional perturbations as well as pure vertical perturbations. In fact, the rotational effect makes the flow more unstable, and hence, turbulence inside the underlying shearing box is inevitable.

In the literature before this work, when the hydrodynamic instability of the Keplerian accretion flow has been studied in the local region, the flow has been approximated to be a plane Couette flow with rotation embedded in it. However, recent works (Nath & Mukhopadhyay 2016; Ghosh & Mukhopadhyay 2020; Razdoburdin 2020) suggested that the presence of an extra force (random or constant) is inevitable in such a flow, at least the effect of an external force is worth exploring. We have therefore argued here that the background flow of a local Keplerian accretion disk will deviate from a plane Couette flow. We have considered here such a deviated background flow modified to the plane Poiseuille flow. This modification depends on the strength of force and the boundary conditions. Controlling these two factors, a plane Couette flow and also its nature can be revived. We know that a plane Poiseuille flow is unstable beyond the respective critical values of certain parameters for planer perturbation. We therefore can argue that the local Keplerian flow becomes unstable due to the presence of an extra force.

However, the effect of the Coriolis force, which is inevitable for a shearing box in the Keplerian disk, makes the problem more interesting. We know that rotation stabilizes the linear shear flow. However, for a plane Poiseuille flow, it has opposite effects. In the presence of rotation, a plane Poiseuille flow becomes unstable at a *Re* that is about two orders of magnitude smaller than that required for the instability without rotation. We have shown here that as the rotation parameter q increases, the flow becomes more unstable (or at least less stable) for a particular set of parameters. The important point here is that the presence of an extra force modifies the local Keplerian flow from linear shear to nonlinear shear, and the Coriolis effect makes it unstable for a very small *Re*. We have also argued that even the presence of a tiny force, that could lead to the required amount of deviation from the linear shear, makes it unstable even in the presence of rotation. When the flow becomes unstable, it is eventually expected to become nonlinear and turbulent. It therefore helps us to understand the subcritical transition to turbulence in a hydrodynamic accretion flow and other laboratory flows where external forcing, however tiny, is unavoidable.

S.G. acknowledges DST India for the INSPIRE fellowship. We are thankful to Laurette S. Tuckerman of the Centre national de la recherche scientifique and Dwight Barkley of the University of Warwick for the discussion that motivated us to initiate this work and further discussion for a better presentation. We also thank Tushar Mondal and Sudeb Ranjan Datta of Indian Institute of Science for their comments and suggestions. We are thankful to the referee for insightful suggestions and comments that helped us present the work in a better way. This work is partly supported by a fund of the Department of Science and Technology (DST-SERB) with research grant No. DSTO/PPH/BMP/1946 (EMR/2017/001226).

Appendix
The Derivation of the Background Flow in the Local Region of the Keplerian Accretion Disk

Let us consider a fluid element inside the box at the point *P*. With respect to *C*, the flow is along the ϕ direction. Inside the

box, however, the flow will be along the y-direction only. Now let us assume that the velocity at P with respect to the box is V_Y. Nevertheless, the velocity at the same point with respect to C would be $R\Omega_0 + V_Y$. Had there been no shearing box, the velocity of the fluid at the point P would be ΩR with respect to C. Hence,

$$\begin{aligned} R\Omega_0 + V_Y &= \Omega R \Rightarrow V_Y = R(\Omega - \Omega_0) \\ &= R(\Omega(R_0 + X) - \Omega(R_0)), \\ &\quad [R - R_0 = X \ll R_0, R] \\ &= R\left[\Omega(R_0) + X\left(\frac{d\Omega}{dR}\right)_{R_0} + \ldots - \Omega(R_0)\right] \\ &\cong RX\left(\frac{d\Omega}{dR}\right)_{R_0} \\ &= -q\Omega_0 X\frac{R}{R_0} \\ &= -q\Omega_0 X\left(1 + \frac{X}{R_0}\right) \\ &\cong -q\Omega_0 X. \end{aligned} \tag{A1}$$

ORCID iDs

Subham Ghosh https://orcid.org/0000-0002-9841-3756
Banibrata Mukhopadhyay https://orcid.org/0000-0002-3020-9513

References

Afshordi, N., Mukhopadhyay, B., & Narayan, R. 2005, ApJ, 629, 373
Alfredsson, P. H., & Persson, H. 1989, JFM, 202, 543
Avila, M. 2012, PhRvL, 108, 124501
Bai, X.-N. 2013, ApJ, 772, 96
Bai, X.-N. 2017, ApJ, 845, 75
Balakumar, P. 1997, ThCFD, 9, 103
Balbus, S. A. 2003, ARA&A, 41, 555
Balbus, S. A., & Hawley, J. F. 1991, ApJ, 376, 214
Balbus, S. A., Hawley, J. F., & Stone, J. M. 1996, ApJ, 467, 76
Bhatia, T. S., & Mukhopadhyay, B. 2016, PhRvF, 1, 063101
Cantwell, C. D., Barkley, D., & Blackburn, H. M. 2010, PhFl, 22, 034101
Chagelishvili, G. D., Zahn, J. P., Tevzadze, A. G., & Lominadze, J. G. 2003, A&A, 402, 401
Chandrasekhar, S. 1960, PNAS, 46, 253
Cowley, S. J., & Smith, F. T. 1985, JFM, 156, 83
Das, U., Begelman, M. C., & Lesur, G. 2018, MNRAS, 473, 2791
Dauchot, O., & Daviaud, F. 1995, PhFl, 7, 335
Driscoll, T. A., Hale, N., & Trefethen, L. N. 2014, Chebfun Guide (Oxford: Pafnuty Publications)
Dubrulle, B., Dauchot, O., Daviaud, F., et al. 2005a, PhFl, 17, 095103
Dubrulle, B., Marié, L., Normand, C., et al. 2005b, A&A, 429, 1
Finlay, W. H. 1990, JFM, 215, 209
Frank, J., King, A., & Raine, D. J. 2002, Accretion Power in Astrophysics (3rd ed.; Cambridge: Cambridge University Press), 398
Gammie, C. F., & Menou, K. 1998, ApJ, 492, L75
Ghosh, S., & Mukhopadhyay, B. 2020, MNRAS, 496, 4191
Ghosh, S., & Mukhopadhyay, B. 2021, PhRvF, 6, 013903
Hains, F. D. 1967, PhFl, 10, 2079
Hawley, J. F., Balbus, S. A., & Winters, W. F. 1999, ApJ, 518, 394
Hawley, J. F., Gammie, C. F., & Balbus, S. A. 1995, ApJ, 440, 742
Ioannou, P. J., & Kakouris, A. 2001, ApJ, 550, 931
Kersale, E., Hughes, D. W., Ogilvie, G. I., Tobias, S. M., & Weiss, N. O. 2004, ApJ, 602, 892
Kim, W.-T., & Ostriker, E. C. 2000, ApJ, 540, 372
Klahr, H. H., & Bodenheimer, P. 2003, ApJ, 582, 869
Klotz, L., Lemoult, G., Frontczak, I., Tuckerman, L. S., & Wesfreid, J. E. 2017, PhRvF, 2, 043904
Lesur, G., & Longaretti, P.-Y. 2005, A&A, 444, 25
Lezius, D. K., & Johnston, J. P. 1976, JFM, 77, 153
Lynden-Bell, D., & Pringle, J. E. 1974, MNRAS, 168, 603
Mahajan, S. M., & Krishan, V. 2008, ApJ, 682, 602
Menou, K. 2000, Sci, 288, 2022
Menou, K., & Quataert, E. 2001, ApJ, 552, 204
Mukhopadhyay, B. 2013, PhLB, 721, 151
Mukhopadhyay, B., Afshordi, N., & Narayan, R. 2005, ApJ, 629, 383
Mukhopadhyay, B., & Chattopadhyay, A. K. 2013, JPhA, 46, 035501
Mukhopadhyay, B., Mathew, R., & Raha, S. 2011, NJPh, 13, 023029
Nath, S. K., & Mukhopadhyay, B. 2015, PhRvE, 92, 023005
Nath, S. K., & Mukhopadhyay, B. 2016, ApJ, 830, 86
Ogilvie, G. I., & Pringle, J. E. 1996, MNRAS, 279, 152
Orszag, S. A. 1971, JFM, 50, 689
Paoletti, M. S., van Gils, D. P. M., Dubrulle, B., et al. 2012, A&A, 547, A64
Papaloizou, J. C. B., & Pringle, J. E. 1984, MNRAS, 208, 721
Pessah, M. E., & Psaltis, D. 2005, ApJ, 628, 879
Razdoburdin, D. N. 2020, MNRAS, 492, 5366
Richard, D., & Zahn, J.-P. 1999, A&A, 347, 734
Rüdiger, G., & Zhang, Y. 2001, A&A, 378, 302
Savenkov, I. V. 2010, CMMPh, 50, 1399
Shakura, N. I., & Sunyaev, R. A. 1973, A&A, 24, 337
Tevzadze, A. G., Chagelishvili, G. D., Zahn, J. P., Chanishvili, R. G., & Lominadze, J. G. 2003, A&A, 407, 779
Velikhov, E. 1959, Zhur. Eksptl'. i Teoret. Fiz., 36
Xiong, X., & Tao, J. 2020, PhFl, 32, 094104
Yecko, P. A. 2004, A&A, 425, 385